

Context-aware Diversity Enhancement for Neural Multi-Objective Combinatorial Optimization

Yongfan Lu¹ Zixiang Di¹ Bingdong Li¹ Shengcui Liu² Hong Qian¹ Peng Yang³ Ke Tang³ Aimin Zhou¹

Abstract

Multi-objective combinatorial optimization (MOCO) problems are prevalent in various real-world applications. Most existing neural MOCO methods rely on problem decomposition to transform an MOCO problem into a series of single-objective combinatorial optimization (SOCO) problems and train attention models based on a single-step and deterministic greedy rollout. However, inappropriate decomposition and undesirable short-sighted behaviors of previous methods tend to induce a decline in diversity. To address the above limitation, we design a Context-aware Diversity Enhancement algorithm named CDE, which casts the neural MOCO problems as conditional sequence modeling via autoregression (node-level context awareness) and establishes a direct relationship between the mapping of preferences and diversity indicator of reward based on hypervolume expectation maximization (solution-level context awareness). Based on the solution-level context awareness, we further propose a hypervolume residual update strategy to enable the Pareto attention model to capture both local and non-local information of the Pareto set/front. The proposed CDE can effectively and efficiently grasp the context information, resulting in diversity enhancement. Experimental results on three classic MOCO problems demonstrate that our CDE outperforms several state-of-the-art baselines.

1. Introduction

Multi-objective combinatorial optimization (MOCO) problems (Ehrgott & Gandibleux, 2000) are commonly seen in various fields, such as communication routing (Fei et al., 2016), logistics scheduling (Zajac & Huber, 2021), etc.

¹East China Normal University ²A*STAR ³Southern University of Science and Technology. Correspondence to: Bingdong Li <bdli@cs.ecnu.edu.cn>.

Typically, an MOCO problem requires the simultaneous optimization of multiple conflicting objectives, where the amelioration of an objective may lead to the deterioration of others. It is therefore desirable to discover a set of optimal solutions for MOCO problems, known as the Pareto optimal set (Yu, 1974). Unfortunately, finding all the Pareto-optimal solutions of an MOCO problem is a challenging task, particularly considering that a single-objective combinatorial optimization (SOCO) problem might already be NP-hard.

Due to the exponentially increasing computational time required for exactly tackling MOCO problems (Ehrgott et al., 2016), heuristic methods have been favored to yield an approximate Pareto set in practice over the past few decades. Although heuristic methods (Herzel et al., 2021) are relatively efficient, they rely on domain-specific knowledge and involve massive iterative search. Recently, inspired by the success of deep reinforcement learning (DRL) in learning neural heuristics for solving SOCO problems, researchers have also explored DRL-based neural heuristics (Li et al., 2020; Lin et al., 2022) for MOCO problems. Typically, parameterized as a deep model, these neural heuristics adopt an end-to-end paradigm to construct solutions without iterative search, significantly reducing computational time compared with traditional heuristic methods.

Existing neural MOCO methods typically decompose an MOCO problem into a series of SOCO subproblems by aggregation functions and then train attention models based on a single-step and deterministic greedy rollout to obtain a Pareto set. This approach can be seen as an extension of decomposition-based multi-objective optimization strategies (Zhang & Li, 2007) to an infinite preference scenario with the aid of REINFORCE. However, previous methods suffer from several drawbacks. Firstly, conventional Markov decision-based neural MOCO algorithms tend to induce undesirable short-sighted behaviors because of the neglect of sequence property (Rybkin et al., 2021), which might lead to over-optimization of an objective and fall into local optimum (Kamalaruban et al., 2020). Secondly, the solutions mapped by different subproblems are tackled independently, which harms diversity since only local term is considered in the reward function and mutual supportiveness of subproblems is largely ignored. Both drawbacks result in the loss

of diversity.

After identifying the above-mentioned challenges, we propose to utilize context information to enhance diversity effectively and efficiently. Specifically, we have extended the idea of sequence modeling (Chen et al., 2021; Janner et al., 2021) and hypervolume expectation maximization (Deng & Zhang, 2019; Zhang & Golovin, 2020; Zhang et al., 2023) to MOCO to obtain node- and solution-level context awareness. The contributions of this work can be summarized as follows: (1) We design a Context-aware Diversity Enhancement algorithm, termed as CDE, which is the first to put forward the ideas of node and solution-level context awareness for MOCO. Node-level context awareness casts the neural MOCO problems as conditional sequence modeling and autoregressively update node embeddings. Solution-level context awareness establishes a direct relationship between the mapping of preferences and diversity indicator of reward based on hypervolume expectation maximization. (2) Based on the solution-level context awareness, we propose a hypervolume residual update (HRU) strategy to make the Pareto attention model grasp both local and non-local information of the PS/PF and avoid being misled by weak solutions to a certain degree. (3) Experimental results on three classic MOCO problems demonstrate that our CDE outperforms state-of-the-art neural baselines by superior decomposition and efficient diversity enhancement.

2. Related Work

Neural Heuristics for MOCO. Decomposition is a mainstream scheme in learning-based methods for multi-objective optimization (Lin et al., 2022; Navon et al., 2020; Lin et al., 2019). Their basic idea is to decompose MOCO problems into multiple subproblems according to prescribed weight vectors, and then train a single model or multiple models to solve these subproblems. For example, (Li et al., 2020) and (Zhang et al., 2021) train multiple models collaboratively through a transfer learning strategy. (Lin et al., 2022) train a hypernetwork-based model to generate the decoder parameters conditioned on the preference for MOCO (PMOCO). Both MDRL (Zhang et al., 2022) and EMNH (Chen et al., 2023a) leverages meta-learning to train a deep reinforcement learning model that could be fine-tuned for various subproblems. NHDE (Chen et al., 2023b) proposes indicator-enhanced DRL with an HGA model, which is the first to introduce the hypervolume into the reward for MOCO to enhance diversity.

Hypervolume Expectation Maximization. The hypervolume indicator measures the quality of MOCO solution sets and is consistent with Pareto dominance. Maximizing hypervolume is a basic principle in multiobjective optimization algorithm design (Emmerich et al., 2005; Zitzler et al.,

2007). Many methods leverage hypervolume maximization to train neural networks. Deist et al. (Deist et al., 2023) adopt the idea of gradient search to obtain a finite set of Pareto solutions. Zhang et al. (Zhang et al., 2023) extends hypervolume scalarization of a finite set (Shang et al., 2018) to hypervolume expectation with a simple MLP. However, in terms of sequential prediction problems, traditional MLP is not suitable and the introduction of hypervolume expectation maximization needs to be further studied.

Sequence Modeling. Sequence modeling excels in capturing temporal dependencies and structured data (Bellemare et al., 2013), providing robust predictions for sequential tasks compared to the trial-and-error nature of traditional Markov decision. Chen et al. (Chen et al., 2021) propose a offline method, termed decision transformer, which is the first to cast the problem of RL as conditional sequence modeling and conditions an autoregressive model on the desired return (reward), past states, and actions. Janner et al. (Janner et al., 2021) proposes trajectory transformer, which further models distributions over trajectories and repurposing beam search as a planning algorithm and demonstrate the flexibility of this approach across long-horizon dynamics prediction, imitation learning and so on.

3. Preliminaries

3.1. Multi-Objective Combinatorial Optimization

Without loss of generality, an MOCO problem can be mathematically stated as follows :

$$\begin{aligned} \min \quad & \mathbf{f}(\mathbf{x}) = (f_1(\mathbf{x}), f_2(\mathbf{x}), \dots, f_m(\mathbf{x}))^T \\ \text{s.t.} \quad & \mathbf{x} \in \mathcal{X} \end{aligned}, \quad (1)$$

where $\mathbf{x} = (x_1, x_2, \dots, x_d)$ is the decision vector, $\mathbf{f}(\cdot)$: $\mathcal{X} \rightarrow \mathcal{T}$ is m objective functions, \mathcal{X} and \mathcal{T} denote the (nonempty) *decision space* and the *objective space*, respectively. Since the objectives are usually in conflict with each other, a set of trade-off solutions is to be sought. The concept of *Pareto optimality* is introduced.

Definition 3.1 (Pareto dominance (Yu, 1974)). Given two solutions \mathbf{a}, \mathbf{b} in the region \mathcal{X} , \mathbf{a} is said to *dominate* \mathbf{b} (denoted as $\mathbf{a} \prec \mathbf{b}$) if and only if $\forall i \in \{1, 2, \dots, m\}, f_i(\mathbf{a}) \leq f_i(\mathbf{b})$ and $\exists j \in \{1, 2, \dots, m\}, f_j(\mathbf{a}) < f_j(\mathbf{b})$.

Definition 3.2 (Pareto optimality). A solution $\mathbf{a}^* \in \mathcal{X}$ is Pareto optimal if no other solution $\mathbf{a} \in \mathcal{X}$ can dominate it.

Definition 3.3 (Pareto Set and Pareto Front). The solution set consisting of all the Pareto optimal solutions is called the *Pareto set* (PS): $PS = \{\mathbf{a} \in \mathcal{X} | \forall \mathbf{b} \in \mathcal{X}, \mathbf{b} \not\prec \mathbf{a}\}$ and the corresponding objective vector set of the PS is the *Pareto front* (PF).

3.2. Performance Evaluation

The nadir/ideal point of an MOCO problem is constructed by the worst/best objective values of the Pareto set $y_i^{nadir} = \sup_{y \in \mathcal{T}} \{y_i\}$ and $y_i^{ideal} = \inf_{y \in \mathcal{T}} \{y_i\}$, $\forall i \in 1, \dots, m$. Given a set of objective vectors Y , the hypervolume (HV) indicator (Zitzler & Thiele, 1999) is defined as follows,

$$\mathcal{HV}_r(Y) = \Lambda(\{q \in \mathbb{R}^d \mid \exists p \in Y : p \preceq q \text{ and } q \preceq r\}), \quad (2)$$

where $\Lambda(\cdot)$ denotes the Lebesgue measure. and r is a reference vector. We require that $r \succeq y^{nadir}$. All methods share the same reference point r for a problem (see Appendix F).

4. Methodology

4.1. Overview

Our context-aware diversity enhancement (CDE) takes the first attempt to cast the neural MOCO problems as conditional sequence modeling and establishes a direct relationship between the mapping between preferences and solutions and hypervolume based on hypervolume expectation maximization (HEM) for neural MOCO, enhancing diversity via context-aware from two aspects (Figure 1 and Algorithm 1). Moreover, we design a hypervolume residual update (HRU) strategy to better grasp local and non-local information and avoid the potential misleading caused by the unequal focus of different preferences. We also introduce an explicit and implicit dual inference (EI²) approach that enhances quality and efficiency, supported by local subset selection acceleration (LSSA).

4.2. Node-level Context Awareness via Sequence Modeling

Given a problem instance s , we sequentially solve its subproblem $i \in \{1, \dots, P\}$. The i -th subproblem is associated with weight polar angle θ^i , which follows uniform distribution $\text{Unif}(\Theta)$: $\Theta = [0, \frac{\pi}{2}]^{m-1}$. Let $\pi^i = (\pi_1^i, \dots, \pi_T^i)$ denotes the obtained solution at step i . Given a fully connected graph of T nodes (cities) with m cost objectives of an MOTSP instance, π denotes a tour that visits each city exactly once and returns to the starting node, and the objective functions are an m -dimensional vector $y(\pi) = (y_1(\pi), \dots, y_m(\pi))$.

The idea of sequence modeling has been applied in many fields. However, there was no attempt to integrate sequence modeling into MOCO previously. In this paper, we conduct the first attempt. We follow the idea of encoder in PMOCO except the update of node embeddings $\{\mathbf{h}_{\pi_1}, \dots, \mathbf{h}_{\pi_n}\}$ in each layer. The decoder models trajectories autoregressively with minimal modification to the decoder in PMOCO. At time step t in MOTSP, the context trajectory consists of two parts: 1) the first selected node embedding π_1 ; 2) the nearest K nodes embeddings $\{\pi_{t-K}, \dots, \pi_{t-1}\}$. Then, the sequence

embedding is represented as $\{\mathbf{h}_{\pi_1}, \mathbf{h}_{\pi_{t-K}}, \dots, \mathbf{h}_{\pi_{t-1}}\}$. The context information of other problems can be found in Appendix J. Eq. 3 defines the attention score, which is normalized as $\tilde{\alpha}$ by softmax,

$$\alpha_{uv} = \frac{(W^Q(\mathbf{h}_{\pi_u} + PE(u)))(W^K(\mathbf{h}_{\pi_v} + PE(v))^T)}{\sqrt{d/H}} \quad (3)$$

$$+ f(\mathbf{h}_{\pi_u} + PE(u), \mathbf{h}_{\pi_v} + PE(v)),$$

$$\tilde{\mathbf{h}}_{\pi_t} = \sum_{v=1}^n (\tilde{\alpha}_{1v} W^V \mathbf{h}_{\pi_v} + \sum_{u=t-K}^{t-1} \tilde{\alpha}_{uv} W^V \mathbf{h}_{\pi_v}). \quad (4)$$

where $PE(\cdot)$ denotes the position embedding, which is important to the sequence modeling. Moreover, $f(\cdot)$ denotes the feedforward neural network, which is introduced to generate a dynamic attention weight of current sequence element and key. The above practice is essential to neural MOCO since the importance of previous node position and order for the next node prediction varies with the change of instance, iteration and so on. Finally, as for the multi-head attention (MHA), $\tilde{\mathbf{h}}_t$ is further computed as follows,

$$\tilde{\mathbf{h}}_{\pi_t} = W^O \text{Concat}(\tilde{\mathbf{h}}_{\pi_{t,1}}, \dots, \tilde{\mathbf{h}}_{\pi_{t,H}}), \quad (5)$$

where $\tilde{\mathbf{h}}_{\pi_t}$ for head $h \in \{1, \dots, H\}$ is obtained according to Eq. 4, which is used for update the node embeddings of the last layer by Add&Norm and FFN. In the traditional MHA, W^Q , W^K , W^V and W^O are independent trainable parameters. Besides, the dynamic learnable parameters W^A is introduced to improve the sensitivity to context information (i.e. attention to the K different nodes) when predicting the current node. The practice can effectively improve 1) contextual relevance; 2) flexibility and adaptability; 3) learning efficiency; 4) robustness to variability (Chen et al., 2021).

4.3. Solution-level Context Awareness via Hypervolume Expectation Maximization

Pareto set learning (PSL) is the mainstream idea of dealing with MOCO currently (Lin et al., 2022), which originates from traditional optimization (Hillermeier, 2001) and aims to learn the whole Pareto set by a model. Current neural MOCO methods tend to leverage weighted-sum (WS) or weighted-Tchebycheff (TCH) aggregation and/or use accurate HV to balance convergence (optimality) and diversity (Lin et al., 2022; Chen et al., 2023b). However, they may overemphasize convergence or improve diversity at the sacrifice of high computational overhead. Thus, we propose a novel solution-level context awareness to formulate PSL based on hypervolume expectation maximization, which is only used with MLP in (Zhang et al., 2023) before.

Here an HV scalarization function is introduced for unbiased estimation of the hypervolume indicator:

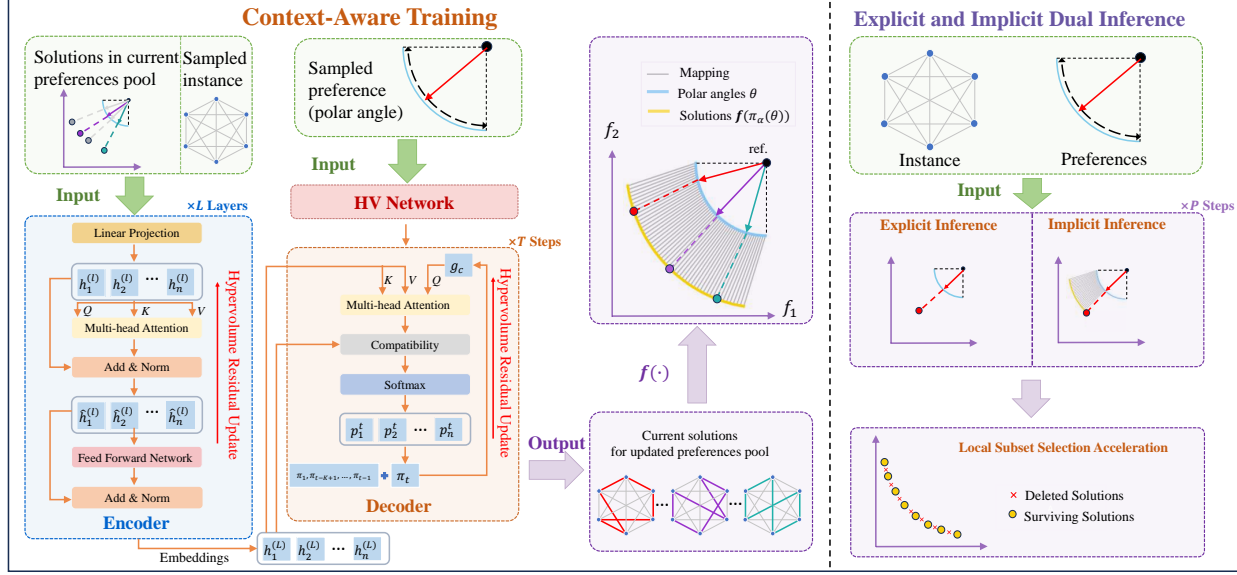


Figure 1. Pipeline of CDE. **Left** (p^t -th training iteration): CDE is trained using a context-aware strategy to establish the mapping between preferences (polar angles) and solutions with effective and efficient diversity enhancement. Specifically, the encoder takes in a sampled instance for projection and solutions generated from previous preferences θ^{p^t-1} offer context information for the current preference θ . In addition, θ generates the decoder parameters through a specifically designed HV network. At step t in the decoder, a context embedding g_c is used to calculate the probability of node selection. The solutions derived from CDE are aligned precisely with the polar angles in a polar coordinate system under mild conditions. **Right**: during inference, CDE employs an explicit and implicit dual inference (EI²) approach to enhance convergence and diversity, and incorporates local subset selection acceleration (LSSA) to enhance efficiency. A well-trained Pareto attention model applies the EI² approach to each polar angle, resulting in solutions with superior convergence and diversity, while LSSA facilitates efficient selection.

Lemma 4.1 (Hypervolume scalarization of a finite set (Shang et al., 2018; Deng & Zhang, 2019; Zhang & Golovin, 2020)). $Y = \{\mathbf{y}^1, \dots, \mathbf{y}^n\}$ denotes set of finite objective vectors and $\mathbf{r} = (r_1, \dots, r_m)$ denotes a reference point, which satisfies $\forall i \in \{1, 2, \dots, m\}, \mathbf{r} \succ \mathbf{y}^i$.

$$\mathcal{HV}_{\mathbf{r}}(Y) := \frac{\Phi}{m2^m} \mathbb{E}_{\theta} \left[\left(\max_{\mathbf{y} \in Y} \{\mathcal{G}^{mtch}(\mathbf{y}|\theta, \mathbf{r})\} \right)^m \right], \quad (6)$$

$$\mathcal{G}^{mtch}(\mathbf{y}|\theta, \mathbf{r}) = \min_{i \in \{1, \dots, m\}} \{(r_i - y_i) / \lambda_i(\theta)\}$$

where $\Phi = \frac{2\pi^{m/2}}{\Gamma(m/2)}$ denotes the area of the $(m-1)$ -D unit sphere, which is a dimension-specific constant and $\Gamma(x) = \int_0^{\inf} z^{x-1} e^{-z} dz$ denotes the analytic continuation of the factorial function. $\lambda(\theta) = (\lambda_1(\theta), \dots, \lambda_m(\theta))$ is the preference vector. It is the Cartesian coordinate of θ on the positive unit sphere \mathbb{S}_+^{m-1} : $\lambda_1(\theta) = \sin \theta_1 \sin \theta_2 \dots \sin \theta_{m-1}, \lambda_2(\theta) = \sin \theta_1 \sin \theta_2 \dots \cos \theta_{m-1}, \dots, \lambda_m(\theta) = \cos \theta_1$.

This scalarization function is a computationally-efficient and accurate estimator of the hypervolume that easily generalizes to higher dimensions. Moreover, it is polynomial in the number of objectives m when \mathcal{X} is suitably compact. This implies that the choice of scalarization functions and polar angles distribution $\text{Unif}(\Theta)$ are theoretically sound and leads to provable convergence to the PF.

Given a set of uniform polar angles, accurately estimating HV with diminutive variance relies on numerous uniformly distributed solutions. However, solutions are not evenly distributed, especially in the nascent stage of optimization. Thus, it is necessary to build a mapping between the preferences (polar angles) and the PS/PF, replacing the finite set Y via a Pareto attention model. In the other words, the Pareto attention model is able to predict nodes (cities) sequentially when given embedded preferences and further maps the node sequence from the instance space to the objective space. To sum up, what we need to realize is the mapping from preference space to objective space, with instance space as a “bridge”. Thus, we follow the idea of hypervolume expectation maximization (Zhang et al., 2023) to construct our Pareto attention model. The detailed method of extending the scope of the input set in Lemma 4.1 to the PF containing an infinite number of objective vectors refers to Appendix G.

Based on the above discussion, it is favorable and feasible to take into account estimated hypervolume with context awareness when training our Pareto attention model $\Psi_{\beta}(\theta, s)$. The update of the model will be discussed thoroughly in the next subsection. One remaining issue is how to generate the preference-conditioned parameters $\beta_{decoder}(\theta)$. We design an HV Network with reference to hypernetwork

(Schmidhuber, 1992; Shamsian et al., 2021; Sarafian et al., 2021), which provides a powerful and efficient way for conditional computation and is widely used in transfer learning (Ying et al., 2018). We use a simple MLP: $\beta_{decoder}(\theta) = \text{MLP}(\lambda|\psi)$ to generate the decoder parameters conditioned on the polar angles, which is the first to take estimated HV into account. In view of this, our method can better capture the global characteristics of the PF. Moreover, our approximate calculation of hypervolume can better reduce time consumption and enhance model robustness. More details can be found in Appendix I. We also derive an alternative form of CDE which uses the ideal point as a reference point and obtains interesting results in Appendix M.

Algorithm 1 The training process of CDE

```

1: Input: preference distribution  $\Theta$ , instance distribution  $S$ , number of training steps  $E$ , maximal size of polar angles pool  $P'$ , batch size  $B$ , instance size  $N$ , length of sequence  $K$ 
2: Initialize the model parameters  $\beta$ 
3: for  $e = 1$  to  $E$  do
4:    $s_i \sim \text{SampleInstance}(S) \quad \forall i \in \{1, \dots, B\}$ 
5:   Initialize  $\mathcal{F}_i^j \leftarrow \emptyset \quad \forall i \forall j \in \{1, \dots, N\}$ 
6:   Initialize  $\theta^0 \leftarrow \emptyset$ 
7:   for  $p' = 1$  to  $P'$  do
8:      $\theta \sim \text{SamplePreference}(\Theta)$ 
9:      $\theta^{p'} \leftarrow \theta^{p'-1} \cup \theta$ 
10:     $\pi_i^j \sim \text{SampleSolution}(Prob_{\beta(\theta)}(\cdot|s_i, \theta), \mathcal{F}_i^j, K)$ 
11:     $\mathcal{V}_\beta(\theta, s_i) \widetilde{\mathcal{H}\mathcal{V}_r}(\beta, \theta^{p'}, s_i) \leftarrow$  Calculate the projection distance and approximate HV by Eq. 11  $\forall i, j$ 
12:     $\alpha_i^j \leftarrow$  Calculate expected HV improvement by Eq. 8  $\forall i, j$ 
13:     $R_i^j \leftarrow$  Calculate the reward by Eq. 7  $\forall i, j$ 
14:     $b_i \leftarrow \frac{1}{N} \sum_{j=1}^n (R_i^j) \quad \forall i$ 
15:     $\nabla(J)(\beta) \leftarrow \frac{1}{Bn} \sum_{i=1}^B \sum_{j=1}^n [(-R_i^j$ 
16:       $- b_i) \nabla_{\beta(\theta)} \log Prob_{\beta(\theta)}(\pi_i^j | s_i, \theta, \mathcal{F}_i^j)]$ 
17:     $\beta \leftarrow \text{Adam}(\beta, \nabla(J)(\beta))$ 
18:     $\mathcal{F}_i^j \leftarrow \mathcal{F}_i^j \cup \{f(\pi_i^j)\} \quad \forall i, j$ 
19:  end for
20: end for
20: Output: The model parameter  $\beta$ 

```

4.4. Hypervolume Residual Update Strategy

Solution-level context awareness via hypervolume expectation maximization is based on the assumption of unequal importance for all subproblems. The assumption further requires the model to pay different attention to each subproblem. In order to enable the Pareto attention model to capture both local and non-local information of the Pareto set/front, we propose a hypervolume residual update (HRU) strategy to conduct more effective training. The reward

function of subproblem i is defined as follows:

$$R_i = \omega \cdot \underbrace{\mathcal{V}_\beta(\theta^i, s)}_{\text{local}} + \alpha \cdot \underbrace{\widetilde{\mathcal{H}\mathcal{V}_r}(\beta, \theta^i, s)}_{\text{non-local}}. \quad (7)$$

Specifically, the reward function is composed of local and non-local terms: the projection distance of the i -th solution with respect to the polar angle θ^i and the approximate hypervolume of all the selected solutions of subproblems 1 to i . The advantage of this combination is that it can balance exploration and exploitation. Each preference update will drive the evolution of the subsequent preferences. However, there is a deviation between the mapping solution of the Pareto attention model and the true solution with given preference and the deviation will decrease with the model training. Therefore, we introduce a local term decay parameter ω , which is set to $1 - \frac{ep}{EP}$, where ep denotes the current epoch and EP denotes the total epochs since the local term is easier to learn than the non-local term. With the iteration of training epochs, our reward function will approach HV. During the training process, weak solutions may make the Pareto attention model misjudge the global information of the Pareto set/front. Based on the above considerations, we propose a novel definition, namely estimated hypervolume improvement (EHVI), which is as follows:

$$\text{EHVI}(\beta, \theta^i, \theta^i, s) = \widetilde{\mathcal{H}\mathcal{V}_r}(\beta, \theta^i, s) - \widetilde{\mathcal{H}\mathcal{V}_r}(\beta, \theta^{i \setminus \{i\}}, s). \quad (8)$$

When $\text{EHVI}(\cdot)$ is negative, we infer that the current polar angle θ^i is mapped to a weak solution. In this case, the model will disregard the non-local term in order to avoid the weak solution from misleading the model. On the other hand, when $\text{EHVI}(\cdot)$ is positive, the non-local term is utilized to transfer valid global information to subsequent solutions. Regarding the above, $\alpha = \lceil \text{EHVI} \rceil$ since $\widetilde{\mathcal{H}\mathcal{V}_r}$ is a normalized value and then $\text{EHVI} \in (-1, 1)$.

4.5. Novel Inference Strategy

Explicit and Implicit Dual Inference (EI²). In the inference phase, for P given preferences, the well-trained model is used to sequentially solve P corresponding subproblems, as shown in Figure 1. In previous preference-conditioned inference approaches, each subproblem is treated separately, and the WS/TCH method is employed to determine the optimal solution. We refer to this approach as explicit inference, as it only considers the current preference directly, often resulting in local optima and producing duplicate solutions for similar preferences. To handle these issues, we design an additional implicit inference module, which aims to maximize EHVI (Eq. 8). Specifically, we infer all the previous subproblems can provide valuable prior information and construct a partial approximate PF for HV estimation. The **EHVI** serves as a suitable indicator to estimate the

relevance and importance of the solution of the current preference based on all the previous preferences, effectively reducing duplicate solutions as **EHVI** tends to zero in such a case. However, this approach may also carry the risk of local optima, as the distribution of subsequent preferences and solutions is unknown. To mitigate this, we propose the explicit and implicit dual inference (EI²) approach to enable the cooperation of both inference strategies, thereby facilitating better approximation of the PS/PF.

Local Subset Selection Acceleration (LSSA). After the EI² approach, several solutions with superior convergence and diversity are obtained. Then, we want to obtain the optimal subset with a given size restriction (usually P). We introduce efficient LSSA (Wang et al., 2022) instead of traditional LSS. LSSA is based on potential energy from the physics domain. The potential energy of a system Q is defined as follows: $E(Q) = \sum_{\mathbf{x}^i \in Q} \sum_{\mathbf{x}^j \in P \setminus \mathbf{x}^i} U(\mathbf{x}^i, \mathbf{x}^j)$, $U(\mathbf{x}^i, \mathbf{x}^j) = \frac{1}{\|\mathbf{x}^i - \mathbf{x}^j\|^c}$, where $\|\cdot\|$ denotes the module and c is a control parameter. Suppose there are k iterations on average for LSS, the overall time complexity in terms of potential energy calculation is $O(n_1^4 mk)$, where n_1 and m denote the size of Q and objective dimensions of each solution.

Since the overall time complexity is too high, an acceleration strategy is adopted by using the properties of both optimization and the potential energy function. Let Q_1 contain current selected solutions while Q_2 contains the unselected ones. The contribution of a selected one $e1(\mathbf{x})$ and an unselected one $e2(\mathbf{x})$ to Q_1 can be defined by $e1(\mathbf{x}) = \sum_{\mathbf{y} \in Q_1 \setminus \mathbf{x}} U(\mathbf{x}, \mathbf{y})$, $e2(\mathbf{x}) = \sum_{\mathbf{y} \in Q_1} U(\mathbf{x}, \mathbf{y})$. Thus, $E(Q_1)$ is equivalent to $\sum_{\mathbf{x} \in Q_1} e1(\mathbf{x})$. Consider one of Q_1 's neighbors $Q_1 \setminus \{\mathbf{x}\} \cup \{\mathbf{y}\}$, we can obtain the difference between the energy values of the two systems by efficient LSSA strategy $\Delta E(Q_1) = e1(\mathbf{x}) - e2(\mathbf{y}) + U(\mathbf{x}, \mathbf{y})$. The time complexity to update $E(Q_1)$ is $O(1)$ and the time complexity of LSS reduces from $O(n_1^4 mk)$ to $O(n_1^2 m + n_1^2 k)$. LSSA strategy can find the optimal subset from the solutions selected by EI² with high efficiency. All details and proofs are provided in Appendix H.

5. Experimental Study

Problems. We conducted comprehensive experiments to evaluate CDE on 3 typical MOCO problems that are commonly studied in the neural MOCO field (Li et al., 2020; Lin et al., 2022), namely multi-objective traveling salesman problem (MOTSP) (Lust & Teghem, 2010), multi-objective capacitated vehicle routing problem (MOCVRP) (Lacomme et al., 2006), and multi-objective knapsack problem (MOKP) (Bazgan et al., 2009). Following the convention in (Lin et al., 2022), we consider the instances with different sizes, i.e. $T = 20/50/100$ for bi-objective TSP (Bi-TSP), tri-

objective TSP (Tri-TSP) and bi-objective CVRP (Bi-CVRP), and $T = 50/100/200$ for bi-objective KP (Bi-KP).

Hyperparameters. We randomly generated 5000 problem instances on the fly in each epoch for training CDE. The optimizer is ADAM with learning rate $\eta = 10^{-4}$ and weight decay 10^{-6} for 200 epochs. The length of sequence K is set to 3/5/8/10 for 20/50/100/200 instance nodes. During training, the maximal size of polar angles pool P' is set to 20 for each instance. During inference, we generate $P = 101$ and $P = 10201$ uniformly distributed preferences (polar angles) for $m = 2$ and $m = 3$, respectively. Besides, we set the control parameter c to $2m$ and set N to T , following (Kwon et al., 2020). All hyperparameter studies can be found in Appendix N.3.

Baselines. We compare CDE with two kinds of state-of-the-art baselines: 1) Traditional heuristics. We introduce a widely-used evolutionary algorithm for MOCO: NSGAII (Deb et al., 2002) is a Pareto dominance-based multiobjective genetic algorithm; LKH (Tinós et al., 2018) and dynamic programming (DP) are employed to solve the weighted-sum (WS) based subproblems for MOTSP and MOKP, denoted as WS-LKH and WS-DP, respectively; PPLS/D-C (Shi et al., 2022) is a specialized MOEA for MOCO with local search techniques. 2) Neural heuristics. DRL-MOA (Li et al., 2020) decomposes a MOCO with different preferences and builds a Pointer Network (Vinyals et al., 2015) to solve each subproblem; PMOCO (Lin et al., 2022) is the first to train a single model for all different preferences simultaneously. NHDE-P (Chen et al., 2023b) proposes an indicator-enhanced deep reinforcement learning method to guide the model, which is the first to take the diversity into consideration in the reward. EMNH (Chen et al., 2023b) leverages meta-learning to train a DRL model that could be fine-tuned for various subproblems.

Metrics. Hypervolume (HV) (Audet et al., 2021) is used for performance evaluation, where a higher HV means a better solution set. The average HV, gaps with respect to CDE, and total running time for 200 random test instances are reported. The best (second-best) results are highlighted in **bold** (underline). All the compared methods share the same reference points (see Appendix F).

5.1. Results and Analysis

The overall comparison results are recorded in Table 1, including the average HV, gap, and total running time for 200 random test instances. Given the same number of preferences, CDE significantly surpasses PMOCO and NHDE-P across all problems and sizes. When instance augmentation (aug.) is equipped, CDE achieves the smallest gap among the methods on most cases except Bi-CVRP100

where DRL-MOA performs better. However, DRL-MOA incurs significantly more training time overhead to prepare multiple models for different weights. Besides, DRL-MOA exhibits significant advantages on problems with extremely imbalanced scales (i.e. Bi-CVRP), as it can more effectively decompose subproblems by utilizing prior information. This advantage becomes more pronounced on instances with larger sizes. In contrast, preference-conditioned methods rely on uniform acquisition of preferences. Anyway, CDE shows superior performance than all the other preference-conditioned methods (e.g. PMOCO and NHDE-P) via its context awareness on Bi-CVRP100. Finally, we believe that CDE has the potential to be further improved by incorporating additional prior information.

Regarding the inference efficiency, CDE generally requires slightly more time compared with PMOCO due to the utilization of LSSA. However, the LSSA demonstrates a notable characteristic of time complexity that remains unaffected by the number of instance nodes, resulting in high efficiency even for larger instances. Furthermore, the time consumption of CDE is significantly lower than that of NHDE-P, since NHDE-P adopts accurate HV calculation and multiple Pareto optima strategy. This is also observed during the training process.

5.2. Ablation and Hyperparameter Studies

To analyze the effect of the HRU strategy, we compare CDE with 4 variants: CDE without non-local term (CDE w/o non-local), CDE without local term (CDE w/o local), CDE with a constant of $\alpha = 1$ (CDE w/o residual) and CDE without local term decay parameter (CDE w/o local decay). Moreover, we compare CDE with CDE without implicit inference (CDE w/o implicit) and CDE without explicit inference (CDE w/o explicit), to study the EI^2 approach. As seen in Table 2. The performance of CDE is impaired when any of the components is ablated. Besides, both local and non-local terms are critical for model training since their absence leads to the top 2 biggest gaps. The introduction of adaptive parameters ω and α can effectively control the focus of the Pareto attention model to make the reward function approach HV. We further study the influence of the length of sequence K . We compare CDE with larger K (10/16 for 50/100 instance nodes) and with no context information ($K = 1$) in Table 2. We find that the past information is useful for MOCO since the performance is significantly worse when $K = 1$. Moreover, longer sequence will not get obvious performance improvement. The phenomenon may be based on one hypothesis that when representing a distribution of policies (i.e. sequence modeling), the context allows the attention model to identify which policy generated the actions, enabling better learning and/or improving the training/inference dynamics, and if the sequence length is too long, it will only provide redundant

information.

Table 2. Effects of HRU strategy and EI^2 approach.

Method	Bi-TSP50		Bi-CVRP50		Bi-KP100		Tri-TSP50	
	HV \uparrow	Gap \downarrow						
CDE w/o non-local	0.6347	0.86%	0.4368	0.25%	0.4521	1.07%	0.4487	0.95%
CDE w/o local	0.6251	2.35%	0.4239	3.14%	0.4416	3.31%	0.4326	4.51%
CDE w/o residual	0.6379	0.36%	0.4361	0.36%	0.4547	0.53%	0.4507	0.53%
CDE w/o local decay	0.6401	0.03%	0.4376	0.04%	0.4566	0.11%	0.4529	0.04%
CDE w larger K	0.6403	0.01%	0.4375	0.53%	0.4572	-0.02%	0.4530	0.02%
CDE w/o context	0.6389	0.37%	0.4356	0.53%	0.4552	0.42%	0.4513	0.40%
CDE w/o implicit	0.6371	0.48%	0.4367	0.27%	0.4558	0.28%	0.4517	0.31%
CDE w/o explicit	0.6363	0.61%	0.4348	0.71%	0.4549	0.48%	0.4511	0.44%
CDE	0.6404	0.00%	0.4379	0.00%	0.4571	0.00%	0.4531	0.00%

5.3. Validity of Context Awareness

As demonstrated earlier, CDE aims to enhance diversity via context awareness for different subproblems and understand their interconnections. In CDE, the node-level context awareness improves the attention model’s understanding of sequence properties and the solution-level context awareness promotes the diversity of PS/PF. The integration of mappings between polar angles (preferences) and solutions approximates the HV. This allows the Pareto attention model to effectively capture these mappings, benefiting from its larger state space compared with traditional heuristic optimization methods. Furthermore, CDE improves previous decomposition-based approaches by building the assumption of unequal importance for all subproblems. As a result, CDE is able to approximate the entire Pareto front and prevent duplicate solutions across different subproblems. Figure 2 visualizes the mapping of CDE and other decomposition-based methods in the objective space.

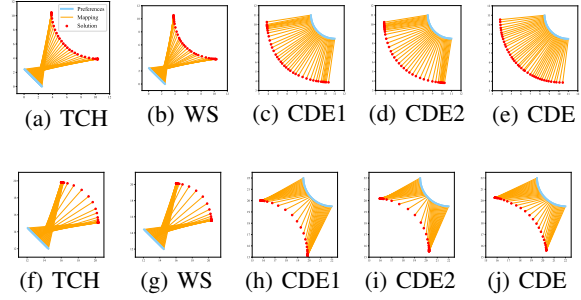


Figure 2. Visual comparisons on Bi-TSP20 (a-e) and Bi-KP50 (f-j). CDE has better adaptability than WS- and TCH-based approaches. CDE1 and CDE2 denote the CDE w/o node-level context awareness and solution-level context awareness, respectively. Any ablation of context-aware components leads to a decrease in diversity.

This visualization supports our idea from two perspectives: 1) Diversity. In terms of the true PF with uniformly distributed solutions (e.g. MOTSP), WS, TCH-based PMOCO, and two CDE variants produce a large number of duplicate solutions at the corner of the PF. In contrast, CDE (Fig.

Table 1. Experimental results on 200 random instances for MOCO problems.

Method	Bi-TSP20			Bi-TSP50			Bi-TSP100		
	HV \uparrow	Gap \downarrow	Time \downarrow	HV \uparrow	Gap \downarrow	Time \downarrow	HV \uparrow	Gap \downarrow	Time \downarrow
WS-LKH (101 pref.)	0.6268	1.10%	4.2m	0.6401	0.55%	41m	0.7071	0.10%	2.6h
PPLS/D-C (200 iter.)	0.6256	1.29%	25m	0.6282	2.40%	2.7h	0.6845	3.30%	11h
NSGAI-II-TSP	0.5941	6.26%	40m	0.5984	7.03%	43m	0.6643	6.15%	53m
DRL-MOA (101 models)	0.6257	1.28%	7s	0.6360	1.18%	10s	0.6971	1.51%	22s
PMOCO (101 pref.)	0.6266	1.14%	8s	0.6349	1.35%	13s	0.6953	1.77%	21s
NHDE-P (101 pref.)	0.6288	0.79%	4.3m	0.6389	0.73%	8.3m	0.7005	1.03%	16m
CDE (101 pref.)	<u>0.6324</u>	<u>0.24%</u>	18s	0.6404	0.53%	23s	0.7014	0.89%	31s
EMNH (aug.)	0.6271	1.05%	1.3m	0.6408	0.44%	4.6m	0.7023	0.78%	17m
PMOCO (101 pref. & aug.)	0.6273	1.03%	46s	0.6392	0.69%	3.1m	0.6997	1.14%	5.7m
NHDE-P (101 pref. & aug.)	0.6296	0.66%	9.8m	<u>0.6429</u>	<u>0.09%</u>	19m	0.7050	0.40%	40m
CDE (101 pref. & aug.)	0.6340	0.00%	1.2m	0.6437	0.00%	4.5m	0.7079	0.00%	6.8m
Method	Bi-CVRP20			Bi-CVRP50			Bi-CVRP100		
PPLS/D-C (200 iter.)	0.3351	4.04%	1.2h	0.4149	3.42%	9.6h	0.4083	1.87%	37h
NSGAI-II-CVRP	0.3123	10.57%	37m	0.3631	15.48%	38m	0.3538	14.97%	43m
DRL-MOA (101 models)	0.3453	1.12%	7s	0.4270	0.61%	20s	0.4176	-0.36%	40s
PMOCO (101 pref.)	0.3467	0.72%	8s	0.4271	0.58%	18s	0.4131	0.72%	36s
NHDE-P (101 pref.)	0.3458	0.97%	1.5m	0.4248	1.12%	3.1m	0.4127	0.82%	5.3m
CDE (101 pref.)	0.3471	0.63%	17s	0.4279	0.47%	31s	0.4143	0.43%	58s
EMNH (aug.)	0.3471	0.60%	33s	0.4250	1.07%	1.4m	0.4146	0.36%	3.7m
PMOCO (101 pref. & aug.)	<u>0.3481</u>	<u>0.32%</u>	1m	<u>0.4287</u>	<u>0.21%</u>	2.1m	0.4150	0.26%	4.5m
NHDE-P (101 pref. & aug.)	0.3465	0.77%	5.1m	0.4262	0.79%	9.2m	0.4139	0.53%	21m
CDE (101 pref. & aug.)	0.3492	0.00%	2.2m	0.4297	0.00%	4.1m	<u>0.4161</u>	<u>0.00%</u>	6.8m
Method	Bi-KP50			Bi-KP100			Bi-KP200		
WS-DP (101 pref.)	0.3563	0.50%	9.5m	0.4531	0.77%	1.2h	0.3599	2.04%	3.7h
PPLS/D-C (200 iter.)	0.3528	1.48%	18m	0.4480	1.88%	46m	0.3541	3.62%	1.4h
NSGAI-II-KP	0.3112	13.10%	30m	0.3514	23.07%	31m	0.3511	4.44%	33m
EMNH	0.3561	0.56%	17s	0.4535	0.68%	53s	0.3603	1.93%	2.3m
DRL-MOA (101 models)	0.3559	0.61%	8s	0.4531	0.77%	13s	0.3601	1.99%	1.1m
PMOCO (101 pref.)	0.3552	0.81%	13s	0.4522	0.96%	19s	0.3595	2.15%	50s
NHDE-P (101 pref.)	<u>0.3564</u>	<u>0.47%</u>	1.1m	<u>0.4541</u>	<u>0.55%</u>	2.5m	<u>0.3612</u>	<u>1.69%</u>	5.3m
CDE (101 pref.)	0.3582	0.00%	21s	0.4571	0.00%	33s	0.3674	0.00%	1.4m
Method	Tri-TSP20			Tri-TSP50			Tri-TSP100		
WS-LKH (210 pref.)	0.4718	1.50%	20m	0.4493	2.50%	3.3h	0.5160	1.28%	11h
PPLS/D-C (200 iter.)	0.4698	1.92%	1.3h	0.4174	9.42%	3.8h	0.4376	16.28%	13h
NSGAI-II-TSP	0.4216	11.98%	2.1h	0.4130	10.37%	2.3h	0.4291	17.91%	2.5h
DRL-MOA (1035 models)	0.4712	1.63%	51s	0.4396	4.60%	1.5s	0.4915	5.97%	3.1s
PMOCO (10201 pref.)	0.4749	0.86%	8.9m	0.4489	2.58%	17m	0.5102	2.39%	34m
NHDE-P (10201 pref.)	0.4764	0.54%	53m	0.4513	2.06%	1.8h	0.5118	2.09%	4.3h
CDE (10201 pref.)	0.4782	0.19%	10m	0.4531	1.71%	19m	0.5129	1.87%	41m
EMNH (aug.)	0.4712	1.63%	7.1m	0.4418	4.12%	58m	0.4973	4.86%	2.4h
PMOCO (10201 pref. & aug.)	0.4757	0.69%	20m	0.4573	0.76%	1.1h	0.5123	1.99%	4.3h
NHDE-P (10201 pref. & aug.)	<u>0.4772</u>	<u>0.38%</u>	2.1h	<u>0.4595</u>	<u>0.28%</u>	6.7h	<u>0.5210</u>	<u>0.33%</u>	15.3h
CDE (10201 pref. & aug.)	0.4791	0.00%	26m	0.4609	0.00%	1.3h	0.5227	0.00%	4.8h

2(e)) realizes uniform mapping on the PF. When examining the true PF with non-uniformly distributed solutions (e.g., MOKP), WS-, TCH-based methods, and two variants struggle to find solutions in sparse regions, while CDE (Fig. 2(j)) effectively simulates the nonuniform distribution characteristics and successfully locates solutions in such areas. 2) Clarity. The mappings generated by CDE exhibit distinct geometric representations compared with other decomposition-based approaches. These observations lead us to conclude that CDE demonstrates exceptional adaptability due to its context awareness and each component plays a positive role in enhancing diversity. More visualization results are presented in Appendix N.4.

6. Conclusion

This paper proposes a Context-aware Diversity Enhancement method for MOCO, offering a novel context-aware perspective, which achieves node-level context awareness via sequence modeling and solution-level context awareness via hypervolume expectation maximization. HRU strategy makes the Pareto attention model better utilize the local and non-local information of the PS/PF. Furthermore, the EI² approach provides high-quality solutions with efficient approximate HV while LSSA enhances selection efficiency. Experimental results on three well-known MOCO problems demonstrate the superiority of CDE, particularly in terms of superior decomposition and efficient diversity enhancement.

Impact Statements. This paper presents work whose goal is to advance the field of Multi-Objective Combinatorial Optimization (MOCO). There are many potential societal consequences of our work, none which we feel must be specifically highlighted here.

References

Audet, C., Bégin, J., Cartier, D., Le Digabel, S., and Salomon, L. Performance indicators in multiobjective optimization. *European journal of operational research*, 292(2):397–422, 2021.

Bazgan, C., Hugot, H., and Vanderpooten, D. Solving efficiently the 0–1 multi-objective knapsack problem. *Computers & Operations Research*, 36(1):260–279, 2009.

Bellemare, M. G., Naddaf, Y., Veness, J., and Bowling, M. The arcade learning environment: An evaluation platform for general agents. *Journal of Artificial Intelligence Research*, 47:253–279, 2013.

Bello, I., Pham, H., Le, Q. V., Norouzi, M., and Bengio, S. Neural combinatorial optimization with reinforcement learning. *arXiv preprint arXiv:1611.09940*, 2016.

Blank, J., Deb, K., Dhebar, Y., Bandaru, S., and Seada, H. Generating well-spaced points on a unit simplex for evolutionary many-objective optimization. *IEEE Transactions on Evolutionary Computation*, 25(1):48–60, 2020.

Borodachov, S. V., Hardin, D. P., and Saff, E. B. *Discrete energy on rectifiable sets*. Springer, 2019.

Chen, J., Wang, J., Zhang, Z., Cao, Z., Ye, T., and Chen, S. Efficient meta neural heuristic for multi-objective combinatorial optimization. *arXiv preprint arXiv:2310.15196*, 2023a.

Chen, J., Zhang, Z., Cao, Z., Wu, Y., Ma, Y., Ye, T., and Wang, J. Neural multi-objective combinatorial optimization with diversity enhancement. *arXiv preprint arXiv:2310.15195*, 2023b.

Chen, L., Lu, K., Rajeswaran, A., Lee, K., Grover, A., Laskin, M., Abbeel, P., Srinivas, A., and Mordatch, I. Decision transformer: Reinforcement learning via sequence modeling. *Advances in neural information processing systems*, 34:15084–15097, 2021.

Deb, K., Pratap, A., Agarwal, S., and Meyarivan, T. A fast and elitist multiobjective genetic algorithm: NSGA-II. *IEEE transactions on evolutionary computation*, 6(2):182–197, 2002.

Deist, T. M., Grewal, M., Dankers, F. J., Alderliesten, T., and Bosman, P. A. Multi-objective learning using hv maximization. In *International Conference on Evolutionary Multi-Criterion Optimization*, pp. 103–117. Springer, 2023.

Deng, J. and Zhang, Q. Approximating hypervolume and hypervolume contributions using polar coordinate. *IEEE Transactions on Evolutionary Computation*, 23(5):913–918, 2019.

Ehrhart, M. and Gandibleux, X. A survey and annotated bibliography of multiobjective combinatorial optimization. *OR-spektrum*, 22:425–460, 2000.

Ehrhart, M., Gandibleux, X., and Przybylski, A. Exact methods for multi-objective combinatorial optimisation. *Multiple criteria decision analysis: State of the art surveys*, pp. 817–850, 2016.

Emmerich, M., Beume, N., and Naujoks, B. An emo algorithm using the hypervolume measure as selection criterion. In *International Conference on Evolutionary Multi-Criterion Optimization*, pp. 62–76. Springer, 2005.

Falcón-Cardona, J. G., Ishibuchi, H., and Coello, C. A. C. Exploiting the trade-off between convergence and diversity indicators. In *2020 IEEE Symposium Series on Computational Intelligence (SSCI)*, pp. 141–148. IEEE, 2020.

Fei, Z., Li, B., Yang, S., Xing, C., Chen, H., and Hanzo, L. A survey of multi-objective optimization in wireless sensor networks: Metrics, algorithms, and open problems. *IEEE Communications Surveys & Tutorials*, 19(1):550–586, 2016.

Florios, K. and Mavrotas, G. Generation of the exact pareto set in multi-objective traveling salesman and set covering problems. *Applied Mathematics and Computation*, 237:1–19, 2014.

Gómez, R. H. and Coello, C. A. C. A hyper-heuristic of scalarizing functions. In *Proceedings of the genetic and evolutionary computation conference*, pp. 577–584, 2017.

Hardin, D. P., Saff, E. B., et al. Discretizing manifolds via minimum energy points. *Notices of the AMS*, 51(10):1186–1194, 2004.

Herzel, A., Ruzika, S., and Thielen, C. Approximation methods for multiobjective optimization problems: A survey. *INFORMS Journal on Computing*, 33(4):1284–1299, 2021.

Hillermeier, C. *Nonlinear multiobjective optimization: a generalized homotopy approach*, volume 135. Springer Science & Business Media, 2001.

Hornik, K., Stinchcombe, M., and White, H. Multilayer feedforward networks are universal approximators. *Neural networks*, 2(5):359–366, 1989.

Janner, M., Li, Q., and Levine, S. Offline reinforcement learning as one big sequence modeling problem. *Advances in neural information processing systems*, 34: 1273–1286, 2021.

Kamalaruban, P., Huang, Y.-T., Hsieh, Y.-P., Rolland, P., Shi, C., and Cevher, V. Robust reinforcement learning via adversarial training with langevin dynamics. *Advances in Neural Information Processing Systems*, 33:8127–8138, 2020.

Kool, W., Van Hoof, H., and Welling, M. Attention, learn to solve routing problems! *arXiv preprint arXiv:1803.08475*, 2018.

Kwon, Y.-D., Choo, J., Kim, B., Yoon, I., Gwon, Y., and Min, S. Pomo: Policy optimization with multiple optima for reinforcement learning. *Advances in Neural Information Processing Systems*, 33:21188–21198, 2020.

Lacomme, P., Prins, C., and Sevaux, M. A genetic algorithm for a bi-objective capacitated arc routing problem. *Computers & Operations Research*, 33(12):3473–3493, 2006.

Li, K., Zhang, T., and Wang, R. Deep reinforcement learning for multiobjective optimization. *IEEE transactions on cybernetics*, 51(6):3103–3114, 2020.

Lin, X., Zhen, H.-L., Li, Z., Zhang, Q.-F., and Kwong, S. Pareto multi-task learning. *Advances in neural information processing systems*, 32, 2019.

Lin, X., Yang, Z., and Zhang, Q. Pareto set learning for neural multi-objective combinatorial optimization. *arXiv preprint arXiv:2203.15386*, 2022.

Lu, H., Zhang, X., and Yang, S. A learning-based iterative method for solving vehicle routing problems. In *International conference on learning representations*, 2019.

Lust, T. and Teghem, J. The multiobjective traveling salesman problem: a survey and a new approach. In *Advances in Multi-Objective Nature Inspired Computing*, pp. 119–141. Springer, 2010.

Ma, Y., Li, J., Cao, Z., Song, W., Zhang, L., Chen, Z., and Tang, J. Learning to iteratively solve routing problems with dual-aspect collaborative transformer. *Advances in Neural Information Processing Systems*, 34:11096–11107, 2021.

Miettinen, K. *Nonlinear multiobjective optimization*, volume 12. Springer Science & Business Media, 1999.

Navon, A., Shamsian, A., Chechik, G., and Fetaya, E. Learning the pareto front with hypernetworks. *arXiv preprint arXiv:2010.04104*, 2020.

Nazari, M., Oroojlooy, A., Snyder, L., and Takáć, M. Reinforcement learning for solving the vehicle routing problem. *Advances in neural information processing systems*, 31, 2018.

Rybkin, O., Zhu, C., Nagabandi, A., Daniilidis, K., Mordatch, I., and Levine, S. Model-based reinforcement learning via latent-space collocation. In *International Conference on Machine Learning*, pp. 9190–9201. PMLR, 2021.

Sarafian, E., Keynan, S., and Kraus, S. Recomposing the reinforcement learning building blocks with hypernetworks. In *International Conference on Machine Learning*, pp. 9301–9312. PMLR, 2021.

Schmidhuber, J. Learning to control fast-weight memories: An alternative to dynamic recurrent networks. *Neural Computation*, 4(1):131–139, 1992.

Shamsian, A., Navon, A., Fetaya, E., and Chechik, G. Personalized federated learning using hypernetworks. In *International Conference on Machine Learning*, pp. 9489–9502. PMLR, 2021.

Shang, K., Ishibuchi, H., Zhang, M.-L., and Liu, Y. A new r_2 indicator for better hypervolume approximation. In *Proceedings of the Genetic and Evolutionary Computation Conference*, pp. 745–752, 2018.

Shi, J., Sun, J., Zhang, Q., Zhang, H., and Fan, Y. Improving pareto local search using cooperative parallelism strategies for multiobjective combinatorial optimization. *IEEE Transactions on Cybernetics*, 2022.

Tinós, R., Helsgaun, K., and Whitley, D. Efficient recombination in the lin-kernighan-helsgaun traveling salesman heuristic. In *Parallel Problem Solving from Nature–PPSN XV: 15th International Conference, Coimbra, Portugal, September 8–12, 2018, Proceedings, Part I 15*, pp. 95–107. Springer, 2018.

Vinyals, O., Fortunato, M., and Jaitly, N. Pointer networks. *Advances in neural information processing systems*, 28, 2015.

Wang, Z., Mao, B., Hao, H., Hong, W., Xiao, C., and Zhou, A. Enhancing diversity by local subset selection in evolutionary multiobjective optimization. *IEEE Transactions on Evolutionary Computation*, 2022.

Ying, W., Zhang, Y., Huang, J., and Yang, Q. Transfer learning via learning to transfer. In *International Conference on Machine Learning*, pp. 5085–5094. PMLR, 2018.

Yu, P.-L. Cone convexity, cone extreme points, and non-dominated solutions in decision problems with multiobjectives. *Journal of optimization Theory and Applications*, 14:319–377, 1974.

Zajac, S. and Huber, S. Objectives and methods in multi-objective routing problems: a survey and classification scheme. *European journal of operational research*, 290(1):1–25, 2021.

Zhang, Q. and Li, H. Moea/d: A multiobjective evolutionary algorithm based on decomposition. *IEEE Transactions on evolutionary computation*, 11(6):712–731, 2007.

Zhang, R. and Golovin, D. Random hypervolume scalarizations for provable multi-objective black box optimization. In *International Conference on Machine Learning*, pp. 11096–11105. PMLR, 2020.

Zhang, X., Lin, X., Xue, B., Chen, Y., and Zhang, Q. Hypervolume maximization: A geometric view of pareto set learning. In *Thirty-seventh Conference on Neural Information Processing Systems*, 2023.

Zhang, Y., Wang, J., Zhang, Z., and Zhou, Y. Modrl/del: multiobjective deep reinforcement learning with evolutionary learning for multiobjective optimization. In *2021 International Joint Conference on Neural Networks (IJCNN)*, pp. 1–8. IEEE, 2021.

Zhang, Z., Wu, Z., Zhang, H., and Wang, J. Meta-learning-based deep reinforcement learning for multiobjective optimization problems. *IEEE Transactions on Neural Networks and Learning Systems*, 2022.

Zitzler, E. and Thiele, L. Multiobjective evolutionary algorithms: a comparative case study and the strength pareto approach. *IEEE transactions on Evolutionary Computation*, 3(4):257–271, 1999.

Zitzler, E., Brockhoff, D., and Thiele, L. The hypervolume indicator revisited: On the design of pareto-compliant indicators via weighted integration. In *Evolutionary Multi-Criterion Optimization: 4th International Conference, EMO 2007, Matsushima, Japan, March 5-8, 2007. Proceedings 4*, pp. 862–876. Springer, 2007.

A. Limitations

The main limitation of CDE is that the design of our reward function is designed by empirical results. In our experiment, we find that both local and non-local term present different influence in different stages of training. To be specific, the non-local term is difficult to study compared with local term while the non-local term contains more information. Therefore, we introduce two adaptive parameters to control the ratio of them according to the state of training. In the future, we will further study the connection between them to design more suitable reward function with theoretically sound.

B. Broader Impact

In our paper, we propose Context-aware Diversity Enhancement algorithm. The positive impact can be analyzed from two aspects. To begin with, we design a novel reward function, which includes local term and non-local term. It is the first time to introduce global information in the reward function. Therefore, the mapping from preferences to objective space in CDE is clearer than the previous methods. Secondly, the introduction of approximate HV can speed up the neural network to extract global information, which has reference significance for the follow-up methods. Lastly, we design a novel inference method compared with previous simple methods.

On the negative side, the reward function without theoretical guarantee shows remarkable improvement in most benchmark problems. However, the performance on real-world engineering design needs to be further tested to ensure safety.

C. Other Related Work

Neural Heuristics for MOCO. Decomposition is a mainstream scheme in learning-based methods for multi-objective optimization (Lin et al., 2022; Navon et al., 2020; Lin et al., 2019). Their basic idea is to decompose MOCO problems into multiple subproblems according to prescribed weight vectors, and then train a single model or multiple models to solve these subproblems. For example, (Li et al., 2020) and (Zhang et al., 2021) train multiple models collaboratively through a transfer learning strategy. (Lin et al., 2022) train a hypernetwork-based model to generate the decoder parameters conditioned on the preference for MOCO (PMOCO). Both MDRL (Zhang et al., 2022) and EMNH (Chen et al., 2023a) leverages meta-learning to train a deep reinforcement learning model that could be fine-tuned for various subproblems. NHDE (Chen et al., 2023b) proposes indicator-enhanced DRL with an HGA model, which is the first to introduce the hypervolume into the reward for MOCO to enhance diversity.

Exact and Heuristic Methods for MOCO. Exact (Florios & Mavrotas, 2014) and heuristic (Herzel et al., 2021) algorithms are two groups of methods to solve MOCO problems in the past decades. The former can find all the Pareto-optimal solutions for only very small-scale problems, while the latter, commonly used in practical applications, can find the approximate Pareto-optimal solutions within a reasonable time. Many multi-objective evolutionary algorithms (MOEAs) are customized for MOCO, including NSGA-II (Deb et al., 2002), MOEA/D (Zhang & Li, 2007), and PPLS/D-C (Shi et al., 2022).

Neural Heuristics for Combinatorial Optimization (CO). In the literature, some end-to-end neural construction methods are developed for solving SOCO problems. The pioneering works (Bello et al., 2016; Nazari et al., 2018; Vinyals et al., 2015) trained a pointer network to construct a near-optimal solution for SOCO problems. Kool et al. ((Kool et al., 2018)) proposed an attention model (AM) based on the transformer architecture. Another representative work is policy optimization with multiple optima (POMO) (Kwon et al., 2020), which exploits the symmetry of solutions to further improve the performance of end-to-end models. Besides, the other line of works, known as neural improvement methods (Ma et al., 2021; Lu et al., 2019), exploited DRL to assist the iterative improvement process from an initial solution, following a learn-to-improve paradigm.

D. Hardware Settings

All the experiments are conducted with an RTX 4090 GPU and a 1.5GHz AMD EPYC 7742 CPU.

E. Aggregation Function

An aggregated (or utility) function can map each point in the objective space into a scalar according to an m -dimensional weight vector λ with $\|\lambda\|_p = 1$ (l_p -norm constraint) and $\lambda_i \geq 0$. Weighted-Sum (WS) and Weighted-Tchebycheff are

commonly used utility functions (Miettinen, 1999). As the simplest representative, WS can be defined by $\min_{\mathbf{x} \in \mathcal{X}} f(\mathbf{x}|\boldsymbol{\lambda}) = \sum_{i=1}^M \lambda_i f_i(\mathbf{x})$.

F. Reference Points and Ideal Points

For a problem, all methods share the same reference point \mathbf{r} and ideal point \mathbf{z} , as shown in Table 3.

Table 3. Description of synthetic benchmarks we used in this work.

Problem	Size	reference point (\mathbf{r})	ideal point (\mathbf{z})
Bi-TSP	20	(20, 20)	(0, 0)
	50	(35, 35)	(0, 0)
	100	(65, 65)	(0, 0)
Bi-CVRP	20	(15, 3)	(0, 0)
	50	(40, 3)	(0, 0)
	100	(60, 3)	(0, 0)
Bi-KP	50	(5, 5)	(30, 30)
	100	(20, 20)	(50, 50)
	200	(30, 30)	(75, 75)
Tri-TSP	20	(20, 20, 20)	(0, 0, 0)
	50	(35, 35, 35)	(0, 0, 0)
	100	(65, 65, 65)	(0, 0, 0)

G. Extension of Lemma 4.1 to Infinite Set

Lemma 4.1 with a finite number of objective vectors can be extended to an infinite set, which can also be expressed as an expectation (Zhang et al., 2023):

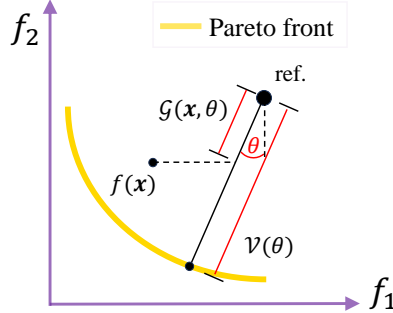


Figure 3. Pareto front hypervolume calculation in the polar coordinate. $\mathcal{G}(\mathbf{x}, \theta)$ is the distance from the reference point to the Pareto front along angle θ . $\mathcal{V}(\theta)$ is the projected distance at angle θ .

$$\mathcal{HV}_{\mathbf{r}}(Y) = \frac{\Phi}{m2^m} \mathbb{E}_{\theta}[(\mathcal{V}_{\mathcal{X}}(\theta)^m)], \quad (9)$$

where $\mathcal{V}_{\mathcal{X}}(\theta)$ denotes the Euclidean distance between the reference point and the PF with the polar angle θ (see Figure 3). Moreover, $\mathcal{V}_{\mathcal{X}}(\theta)$ can be precisely evaluated using the following equation:

$$\mathcal{V}_{\mathcal{X}}(\theta) = \max_{\mathbf{x} \in \mathcal{X}} \mathcal{G}^{mtch}(f(\mathbf{x}), \theta) = \max_{\mathbf{x} \in \mathcal{X}} \min_{i \in \{1, \dots, m\}} \{(r_i - f_i(x_i)) / \lambda_i(\theta)\}, \quad (10)$$

where $\mathcal{G}^{mtch}(f(\mathbf{x}), \theta)$ represents the projected distance of an objective vector $f(\mathbf{x})$ with polar angle θ (see Figure 3). Moreover, the optimal solution \mathbf{x} of $\mathcal{V}_{\mathcal{X}}(\theta)$ has the following properties: 1) satisfies $\frac{r_1 - y_1(\mathbf{x})}{\lambda_1(\theta)} = \dots = \frac{r_m - f_m(\mathbf{x})}{\lambda_m(\theta)}$; 2) is

Pareto optimal. Directly optimizing \mathcal{HV}_r in Eq. 2 is challenging (time-consuming). However, (Zhang et al., 2023) provides an easy-to-compute form of the HV, denoted by $\widetilde{\mathcal{HV}}_r(\beta)$:

$$\begin{aligned}\widetilde{\mathcal{HV}}_r(\beta, \boldsymbol{\theta}^{P'}, s) &= \frac{\Phi}{m2^m} \mathbb{E}_{\boldsymbol{\theta}^{P'}} [(\mathcal{V}_\beta(\theta^i, s))^m], \\ \mathcal{V}_\beta(\theta, s) &= \max(\mathcal{G}^{mtch}(f(\Psi_\beta(\theta, s)), \theta), 0)\end{aligned}\quad (11)$$

where $\boldsymbol{\theta}^{P'} = \{\theta^1, \dots, \theta^{P'}\}$ denotes the polar angles for all the subproblems in the polar angles pool, $\mathcal{V}_\beta(\theta, s)$ is the projected distance in Eq. 10 ($0 \leq \mathcal{V}_\beta(\theta, s) \leq \mathcal{V}_\mathcal{X}(\theta)$ if there is an optimal solution in \mathcal{X}). When the Pareto attention model is well-trained, $\mathcal{V}_\beta(\theta, s) \rightarrow \mathcal{V}_\mathcal{X}(\theta)$, $\forall \theta \in \text{Unif}(\Theta)$ and thus $\widetilde{\mathcal{HV}}_r(\beta) \rightarrow \mathcal{HV}_r(Y)$.

H. Details of Local Subset Selection Acceleration

H.1. Local Subset Selection

For an optimization problem $S^* = \arg \min_{S \in \Omega} f(S)$, where S denotes a subset, Ω denotes the search space and $f(\cdot)$ denotes quantization function of subset quality, a general procedure of a local selection algorithm can be summarized as follows:

1. Select an initial subset S ;
2. Define the neighborhood $\mathcal{N}(S) \subset \Omega$;
3. Move to a neighbor $S \leftarrow S' \in \mathcal{N}(S)$ if $f(S') < f(S)$;
4. Go to step 2 if the termination condition is not met; otherwise, output S .

Definition H.1 (Neighborhood). In our case, a solution S in a local selection is actually a set that contains μ solutions of the multi-objective problems, the search space $\Omega = \{S | S \subset Q, |S| = \mu\}$ contains all the subsets of the given population Q with size μ . It is clear that $|\Omega| = C_{\mu+\lambda}^\mu$. Define the distance between S and S' as the size of their symmetric difference:

$$dis(S, S') = |\{\mathbf{x} | \mathbf{x} \in S, \mathbf{x} \notin S'\} \cup \{\mathbf{x} \in S', \mathbf{x} \notin S\}|. \quad (12)$$

Then, the neighborhood of S can be defined as follows:

$$\mathcal{N}(S) = \{S' | dis(S, S') \leq \epsilon, S' \in \Omega\}, \quad (13)$$

where ϵ is a threshold that defines the range of the neighborhood of S . It is clear that the minimum value of ϵ is 2, and in such case the size of the neighborhood is $|\mathcal{N}(S)| = \mu \times \lambda$. In this article, we only consider the situation when $\epsilon = 2$. In such case, the neighborhood can be also formulated as follows:

$$\mathcal{N}(S) = \{S \setminus \{\mathbf{x}\} \cup \{\mathbf{x}'\} | \mathbf{x} \in S, \mathbf{x}' \in P \setminus S\}. \quad (14)$$

In implementation, we can enumerate all the neighbor solutions of S by replacing an element with another one from the set $Q \setminus S$.

Algorithm 2 presents the proposed subset selection based on a local search. In line 2, the initial subset is generated by using the parent solutions; in line 5, the best neighbor of P^* is found by enumerating all of its neighbors; in lines 6–8, the subset moves to its neighbor if a better one is found; the algorithm terminates in line 10 when no better neighbor could be found, and a local optimal subset is guaranteed.

H.2. Advantages of Potential Energy Function

The potential energy model has been widely used in discretizing manifolds (Hardin et al., 2004; Borodachov et al., 2019). Recently, several traditional optimization researchers tried to adopt similar ideas to improve the diversity of solutions (Falcón-Cardona et al., 2020; Gómez & Coello, 2017) and/or to generate well-distributed reference points (Blank et al., 2020), since it has the following properties.

Algorithm 2 Local Subset Selection

```

1: Input: the given population  $Q_1$ , quantization function of subset quality  $f$ 
2: Generate an initial subset  $Q^* \subset Q_1$ 
3: Set  $Q_2 = Q_1 \setminus Q^*$ 
4: while True do
5:   Set  $x, y = \arg \min_{x \in Q^*, y \in Q_2} f(Q^* \setminus \{x\} \cup \{y\})$ 
6:   if  $f(Q^* \setminus \{x\} \cup \{y\}) < f(Q^*)$  then
7:      $Q^* = Q^* \setminus \{x\} \cup \{y\}$ 
8:      $Q_2 = Q_2 \setminus \{y\} \cup \{x\}$ 
9:   else
10:    Output  $Q^*$  and stop
11:   end if
12: end while
13: Output: the optimal subset  $Q^*$ 

```

1. High Sensitivity: It is highly sensitive to data distribution. A local unevenness of solutions will intensely contribute to the overall metric value, so it could provide strong guidance for the spacing of solutions, providing high selection pressure;
2. Low Computing Complexity: Compared with the HV metric, the potential energy of a system is easy to calculate. An accurate value can be calculated with a time complexity of $O(n_1^2 m)$. Besides, it satisfies the following additional rule, which favors the calculation:

$$\begin{cases} E_{x \notin Q}(Q \cup \{\mathbf{x}\}) = E(Q) + 2 \sum_{\mathbf{y} \in Q} U(\mathbf{y}, \mathbf{x}) \\ E_{x \in Q}(Q \setminus \{\mathbf{x}\}) = E(Q) - 2 \sum_{\mathbf{y} \in Q, \mathbf{y} \neq \mathbf{x}} U(\mathbf{y}, \mathbf{x}) \end{cases} \quad (15)$$

3. Geometric Insensitive: The minimal energy configuration is shape-insensitive, which means uniformly distributed solutions can be obtained regardless of the shape of the optimal PF by minimizing the potential energy.

For these reasons, our algorithm uses the potential energy function as the subset selection objective, i.e., $f(S) = E(S)$. Moreover, We recommend using $c = 2m$ in this article via ablation study.

H.3. Proofs of the Difference of Contributions Between Solutions

Q_1 contains currently selected solutions and Q_2 contains the unselected ones. Then, the contribution of a selected one $e1(\mathbf{x})$ and an unselected one $e2(\mathbf{x})$ according to the systems Q_1 can be defined as follows:

$$\begin{cases} e1(\mathbf{x}) = \sum_{\mathbf{y} \in Q_1 \setminus \mathbf{x}} U(\mathbf{x}, \mathbf{y}) \\ e2(\mathbf{x}) = \sum_{\mathbf{y} \in Q_1} U(\mathbf{x}, \mathbf{y}) \end{cases} \quad (16)$$

Also, The potential energy of a system Q is defined as follows:

$$\begin{aligned} E(Q) &= \sum_{\mathbf{x}^i \in Q} \sum_{\mathbf{x}^j \in P \setminus \mathbf{x}^i} U(\mathbf{x}^i, \mathbf{x}^j), \\ U(\mathbf{x}^i, \mathbf{x}^j) &= \frac{1}{\|\mathbf{x}^i - \mathbf{x}^j\|^c} \end{aligned} \quad (17)$$

Thus, induced from Eq. 17 and Eq. 16, the following equality always holds:

$$E(P \setminus \{\mathbf{x}\} \cup \{\mathbf{y}\}) = E(P) - e1(\mathbf{x}) + e2(\mathbf{y}) - U(\mathbf{x}, \mathbf{y}). \quad (18)$$

Consider one of Q_1 's neighbors $Q_1 \setminus \{\mathbf{x}\} \cup \{\mathbf{y}\}$, where $\mathbf{x} \in Q_1$ and $\mathbf{y} \in Q_2$. We can have the following proof for the difference between the energy of Q_1 and $Q_1 \setminus \{\mathbf{x}\} \cup \{\mathbf{y}\}$:

$$\begin{aligned}
 \Delta E(Q_1) &= E(Q_1) - E(Q_1 \setminus \{\mathbf{x}\} \cup \{\mathbf{y}\}) \\
 &= E(Q_1) - \sum_{\mathbf{x}' \in Q_1 \setminus \{\mathbf{x}\} \cup \{\mathbf{y}\}} \sum_{\mathbf{x}'' \in Q_1 \setminus \{\mathbf{x}, \mathbf{x}'\} \cup \{\mathbf{y}\}} U(\mathbf{x}', \mathbf{x}'') \\
 &= E(Q_1) - \left(\sum_{\mathbf{x}' \in Q_1} \sum_{\mathbf{x}'' \in Q_1 \setminus \{\mathbf{x}'\}} U(\mathbf{x}', \mathbf{x}'') - \sum_{\mathbf{x}' \in Q_1 \setminus \{\mathbf{x}\}} U(\mathbf{x}, \mathbf{x}') + \sum_{\mathbf{x}' \in Q_1} U(\mathbf{y}, \mathbf{x}') - U(\mathbf{x}, \mathbf{y}) \right) \quad (19) \\
 &= E(Q_1) - (E(Q_1) - e1(\mathbf{x}) + e2(\mathbf{y}) - U(\mathbf{x}, \mathbf{y})) \\
 &= e1(\mathbf{x}) - e2(\mathbf{y}) + U(\mathbf{x}, \mathbf{y}).
 \end{aligned}$$

It is clear that when evaluating the neighbor of Q_1 by replacing \mathbf{x} by \mathbf{y} , it is not necessary to calculate the energy of the new system. Instead, only the difference between the energy values of the two systems is needed. \square

Similarly, we can calculate the difference between the contributions of selected and unselected solutions.

Considering a solution $\mathbf{x}' \in Q_1$, if $\mathbf{x}' \neq \mathbf{x}$, we can have following proof:

$$\begin{aligned}
 \Delta e1(\mathbf{x}') &= \sum_{\mathbf{x}'' \in Q_1 \setminus \{\mathbf{x}'\}} U(\mathbf{x}', \mathbf{x}'') - \sum_{\mathbf{x}'' \in Q_1 \setminus \{\mathbf{x}', \mathbf{x}\} \cup \{\mathbf{y}\}} U(\mathbf{x}', \mathbf{x}'') \\
 &= \left(\sum_{\mathbf{x}'' \in Q_1 \setminus \{\mathbf{x}', \mathbf{x}\}} U(\mathbf{x}', \mathbf{x}'') + U(\mathbf{x}', \mathbf{x}) \right) - \left(\sum_{\mathbf{x}'' \in Q_1 \setminus \{\mathbf{x}', \mathbf{x}\}} U(\mathbf{x}', \mathbf{x}'') + U(\mathbf{x}', \mathbf{y}) \right) \quad (20) \\
 &= U(\mathbf{x}', \mathbf{x}) - U(\mathbf{x}', \mathbf{y}).
 \end{aligned}$$

If $\mathbf{x}' = \mathbf{x}$:

$$\begin{aligned}
 \Delta e1(\mathbf{x}') &= \sum_{\mathbf{x}'' \in Q_1 \setminus \{\mathbf{x}'\}} U(\mathbf{x}', \mathbf{x}'') - \sum_{\mathbf{x}'' \in Q_1 \setminus \{\mathbf{x}'\} \cup \{\mathbf{y}\}} U(\mathbf{x}', \mathbf{x}'') \\
 &= \sum_{\mathbf{x}'' \in Q_1 \setminus \{\mathbf{x}'\}} U(\mathbf{x}', \mathbf{x}'') - \left(\sum_{\mathbf{x}'' \in Q_1 \setminus \{\mathbf{x}'\}} U(\mathbf{x}', \mathbf{x}'') + U(\mathbf{x}', \mathbf{y}) \right) \quad (21) \\
 &= -U(\mathbf{x}', \mathbf{y}).
 \end{aligned}$$

Considering a solution $\mathbf{y}' \in Q_2$, if $\mathbf{y}' \neq \mathbf{y}$, we can have following proof:

$$\begin{aligned}
 \Delta e2(\mathbf{y}') &= \sum_{\mathbf{x}'' \in Q_1} U(\mathbf{y}', \mathbf{x}'') - \sum_{\mathbf{x}'' \in Q_1 \setminus \{\mathbf{x}\} \cup \{\mathbf{y}\}} U(\mathbf{y}', \mathbf{x}'') \\
 &= \sum_{\mathbf{x}'' \in Q_1} U(\mathbf{y}', \mathbf{x}'') - \left(\sum_{\mathbf{x}'' \in Q_1} U(\mathbf{y}', \mathbf{x}'') - U(\mathbf{y}', \mathbf{x}) + U(\mathbf{y}', \mathbf{y}) \right) \quad (22) \\
 &= U(\mathbf{y}', \mathbf{x}) - U(\mathbf{y}', \mathbf{y}).
 \end{aligned}$$

If $\mathbf{y}' = \mathbf{y}$:

$$\begin{aligned}
 \Delta e2(\mathbf{y}') &= \sum_{\mathbf{x}'' \in Q_1} U(\mathbf{y}', \mathbf{x}'') - \sum_{\mathbf{x}'' \in Q_1 \setminus \{\mathbf{x}\}} U(\mathbf{y}', \mathbf{x}'') \\
 &= \sum_{\mathbf{x}'' \in Q_1} U(\mathbf{y}', \mathbf{x}'') - \left(\sum_{\mathbf{x}'' \in Q_1} U(\mathbf{y}', \mathbf{x}'') - U(\mathbf{y}', \mathbf{x}) \right) \quad (23) \\
 &= U(\mathbf{y}', \mathbf{x}).
 \end{aligned}$$

In summary:

$$\begin{aligned}\Delta e1(\mathbf{x}') &= \begin{cases} U(\mathbf{x}', \mathbf{x}) - U(\mathbf{x}', \mathbf{y}), & \mathbf{x}' \in Q_1 \setminus \{\mathbf{x}\} \\ -U(\mathbf{x}', \mathbf{y}), & \mathbf{x}' = \mathbf{x} \end{cases} \\ \Delta e2(\mathbf{y}') &= \begin{cases} U(\mathbf{y}', \mathbf{x}) - U(\mathbf{y}', \mathbf{y}), & \mathbf{y}' \in Q_2 \setminus \{\mathbf{y}\} \\ U(\mathbf{y}', \mathbf{x}), & \mathbf{y}' = \mathbf{y} \end{cases}.\end{aligned}\quad (24)$$

□

I. Model Architecture

The core architecture of the base model is similar with POMO, composed of an encoder and a decoder. For node features $\mathbf{x}_1, \dots, \mathbf{x}_n$ and previous solutions \mathcal{F} , the encoder first computes initial node embeddings $\mathbf{h}_1^{(0)}, \dots, \mathbf{h}_n^{(0)} \in \mathcal{R}^d (d = 128)$ and previous solution information by a linear projection. The final node embeddings $\mathbf{h}_1^{(L)}, \dots, \mathbf{h}_n^{(L)}$ are further computed by $L = 6$ attention layers. Each attention layer is composed of a multi-head attention (MHA) with $M = 8$ heads and fully connected feed-forward sublayer. Each sublayer adds a skip-connection and batch normalization, as follows:

$$\mathbf{h}_i^{(l)} = \text{BN}(\hat{\mathbf{h}}_i + \text{FF}(\hat{\mathbf{h}}_i)). \quad (25)$$

The decoder sequentially chooses a node according to a probability distribution produced by the node embeddings to construct a solution. The total decoding step T is determined by the specific problem. The HV network is employed to tackle the preference θ for the corresponding subproblem. Specifically, according to the given θ , the HV network generates the decoder parameters of the MHA model β , which is an encoder-decoder-styled architecture, i.e., $\beta(\theta, s) = [\beta_{en}(s), \beta_{de}(\pi)]$. The HV network adopts a simple MLP model with two 256-dimensional hidden layers and ReLu activation. The MLP first maps an input with $M + 2$ dimensions to a hidden embedding $g(\theta)$, which is then used to generate the decoder parameters by linear projection. At step t in the decoding procedure, the glimpse \mathbf{q}_c of the context embedding \mathbf{g}_c is computed by the MHA layer. Then, the compatibility u is calculated as follows,

$$u_i = \begin{cases} -\infty, & \text{node } i \text{ is masked} \\ C \cdot \tanh\left(\frac{\mathbf{q}_c^T (W^K \mathbf{h}_u^{(L)})}{\sqrt{d/Y}}\right), & \text{otherwise} \end{cases}. \quad (26)$$

where C is set to 10 (Kool et al., 2018). Finally, softmax is employed to calculate the selection probability distribution $\text{Prob}_\beta(\pi|s, \theta^i, \mathcal{F}_i^j)$ for nodes, i.e., $\text{Prob}_\beta(\pi_t|\pi_{1:t-1}, s, \theta^i, \mathcal{F}_i^j) = \text{Softmax}(u)$.

J. Node Features and Context Embedding

The input dimensions of the node features vary with different problems. The inputs of the m -objective TSP are T nodes with $2m$ -dimensional features. The inputs of Bi-CVRP are T customer nodes with 3-dimensional features and a depot node with 2-dimensional features. The inputs of Bi-KP are T nodes with 3-dimensional features. At step t in the decoder, a context embedding \mathbf{g}_c is used to calculate the probability of node selection. For MOTSP, \mathbf{g}_c is defined as the embedding of the first node \mathbf{h}_{π_1} , and the nearest K nodes embeddings $\{\mathbf{h}_{\pi_{t-K}}, \dots, \mathbf{h}_{\pi_{t-1}}\}$. For MOCVRP, \mathbf{g}_c is defined as the nearest K nodes embeddings $\{\mathbf{h}_{\pi_{t-K}}, \dots, \mathbf{h}_{\pi_{t-1}}\}$, and the remaining vehicle capacity. For MOKP, \mathbf{g}_c is defined as the nearest K nodes embeddings $\{\mathbf{h}_{\pi_{t-K}}, \dots, \mathbf{h}_{\pi_{t-1}}\}$ and the remaining knapsack capacity.

A masking mechanism is adopted in each decoding step to ensure the feasibility of solutions. For MOTSP, the visited nodes are masked. For MOCVRP (MOKP), besides the visited nodes, those with a demand (weight) larger than the remaining vehicle (knapsack) capacity are also masked.

K. Inference Process of CDE

In terms of the inference process of CDE, we have adopted explicit and implicit dual inference (line 11-12) in 3 to generate solutions and applied local subset selection acceleration strategy to select elite solutions.

Algorithm 3 The inference process of CDE

```

1: Input: preference distribution  $\Theta$ , instance distribution  $\mathcal{S}$ , number of uniformly distributed preferences (polar angles)  $P$ ,  

   batch size  $B$ , instance size  $N$ , model parameter  $\beta$ , length of sequence  $K$ 
2:  $Pref \leftarrow P$  uniformly distributed preferences are generated according to  $\Theta$ .
3:  $s_i \sim \text{SampleInstance}(\mathcal{S}) \quad \forall i \in \{1, \dots, B\}$ 
4: Initialize  $\mathcal{F}_i^j \leftarrow \emptyset \quad \forall i \forall j \in \{1, \dots, N\}$ 
5: Initialize  $\theta^0 \leftarrow \emptyset$ 
6: Initialize  $\mathbf{Y} \leftarrow \emptyset$ 
7: for  $p = 1$  to  $P$  do
8:    $\theta^p \leftarrow \theta^{p-1} \cup Pref_p$ 
9:    $\pi_i^j \sim \text{SampleSolution}(Prob_{\beta(\theta)}(\cdot | s_i, \theta), \mathcal{F}_i^j, K)$ 
10:   $\mathcal{V}_\beta(\theta, s_i, \widetilde{\mathcal{H}\mathcal{V}_r}(\beta, \theta^{p'}, s_i) \leftarrow \text{Calculate the projection distance and approximate HV by Eq. 11} \quad \forall i, j$ 
11:   $\alpha_i^j \leftarrow \text{Calculate expected HV improvement by Eq. 8} \quad \forall i, j$ 
12:   $R_{i,1}^j \leftarrow \text{Calculate the reward only by the local term of Eq. 7} \quad \forall i, j // \text{Explicit inference}$ 
13:   $R_{i,2}^j \leftarrow \text{Calculate the reward by both the local and the non-local term of Eq. 7 according to parameter } \alpha_i^j \quad \forall i, j // \text{Implicit inference}$ 
14:   $\pi_{i,1}, \pi_{i,2} \leftarrow \text{Argmax}(R_{i,1}^j), \text{Argmax}(R_{i,2}^j) \quad \forall j$ 
15:   $\mathcal{F}_i^j \leftarrow \mathcal{F}_i^j \cup \{\mathbf{f}(\pi_{i,1}), \mathbf{f}(\pi_{i,2})\} \quad \forall i, j$ 
16:   $\mathbf{Y} \leftarrow \mathbf{Y} \cup \{\frac{1}{B} \sum_{i=1}^B \mathbf{f}(\pi_{i,1}), \sum_{i=1}^B \mathbf{f}(\pi_{i,2})\} \quad \forall i$ 
17: end for
18:  $\mathbf{Y} \leftarrow \text{LSSA}(\mathbf{Y})$ 
19: Output: The final solution set  $\mathbf{Y}$ 

```

L. Instance Augmentation

Instance augmentation exploits multiple efficient transformations for the original instance that share the same optimal solution. Then, all transformed problems are solved and the best solution among them are finally selected. According to POMO, a 2D coordinate (x, y) has eight different transformations, $\{(x, y), (y, x), (x, 1 - y), (y, 1 - x), (1 - x, y), (1 - y, x), (1 - x, 1 - y), (1 - y, 1 - x)\}$. An instance of Bi-CVRP has 8 transformations, and an instance of m -objective TSP has 8^m transformations (Lin et al., 2022) due to the full transformation permutation of m groups of 2-dimensional coordinates,.

M. An Alternative Form of CDE

We also provide an alternative surrogate hypervolume function, denoted as CDE-alter. Figure 4 shows details. We first define region S as the set of points dominating the Pareto front.

$$S = \{q | \exists p \in \mathcal{T} : p \prec q \quad \text{and} \quad q \succ p^{ideal}\}. \quad (27)$$

We use the notation $\Lambda(\cdot)$ to represent the Lebesgue measure of a set. Geometrically, as illustrated in Figure 4, it can be observed that:

$$\Lambda(S) + \mathcal{H}\mathcal{V}_r(Y) = \prod_{i=1}^m (r_i - z_i). \quad (28)$$

The volume of S can be calculated in a polar coordinate as follows,

$$\Lambda(S) = \frac{\Phi}{m2^m} \int_{(0, \frac{\pi}{2})^{(m-1)}} \bar{\mathcal{V}}(\theta). \quad (29)$$

Thus, the Pareto hypervolume can be estimated as the volume difference between the regions dominating r and those that

dominate the Pareto front. CDE-alter maximizes the following objective,

$$\begin{aligned}\widetilde{\mathcal{H}\mathcal{V}}_r(\beta, \theta^P, s) &= \prod_{i=1}^m (r_i - z_i) - \frac{\Phi}{m2^m} \mathbb{E}_{\theta^P}[(\bar{\mathcal{V}}_\beta(\theta^i, s))^m], \\ \bar{\mathcal{V}}_\beta(\theta, s) &= \max(\bar{\mathcal{G}}^{mtch}(f(\Psi_\beta(\theta, s)), \theta), 0)\end{aligned}\quad (30)$$

where $\bar{\mathcal{G}}^{mtch}(\cdot)$ is an alternative projected distance function:

$$\bar{\mathcal{G}}^{mtch}(f(\Psi_\beta(\theta, s)), \theta) = \max_{i \in \{1, \dots, m\}} \{(y_i - z_i)/\lambda_i(\theta)\}. \quad (31)$$

Although the Pareto neural model $\Psi_\beta(\cdot)$ theoretically has the ability to represent the complete Pareto set (Hornik et al.,

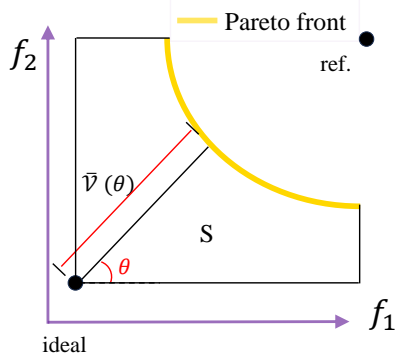


Figure 4. Alternative Pareto front hypervolume calculation in the polar coordinate.

1989), empirical results show that the quality of the learned solutions is sensitive to the specific choice: Eq. 11 and Eq. 30 give different performances on various tasks. The main results of CDE-alter can be found in Appendix N.1.

N. Additional experiments

N.1. Main results of CDE-alter and Analysis

As introduced in Appendix M, we provide an alternative form of CDE, namely CDE-alter. Figure 4 shows the results of CDE-alter compared with several baselines. CDE-alter also shows the best overall performance. Here, we want to discuss the nature of CDE and CDE-alter since they show different features on various problems. Specifically, CDE-alter can show better performance on concave Pareto front (i.e. MOKP), while CDE-alter can show better performance on non-concave Pareto front (i.e. MOTSP and MOCVRP). In terms of non-concave Pareto front, the projection distance $\mathcal{V}_\beta(\theta)$ is uniformly distributed, which provides robustness for training model, while $\bar{\mathcal{V}}_\beta(\theta)$ is sensitive because of its non-uniform distribution which may lead to the overfitting of Pareto attention model. This phenomenon is the opposite on the question concave Pareto front. Therefore, it is necessary to choose different alternatives for specific problems.

N.2. Generalization Study of CDE and CDE-alter

To assess the generalization capability of CDE and CDE-alter. We compare them with the other baselines on 200 random Bi-TSP instances with larger sizes, i.e., Bi-TSP150/200. The comparison results are demonstrated in Table 5. CDE and CDE-alter outperform the state-of-the-art MOEA (i.e., PPLS/D-C) and other neural methods significantly, in terms of HV, which means a superior generalization capability. Note that WS-LCK has a slight advantage over CDE and CDE-alter at the sacrifice of Dozens of times the inference time (i.e. 1.2 hours vs 4.6 minutes). Besides, CDE is superior to CDE-alter on both problems, which also Verifies our idea in Appendix N.1.

N.3. More Hyperparameter Studies

We further study the effects of P' (maximal size of polar angles pool) and c (control parameter of potential energy).

Table 4. Experimental results on 200 random instances for MOCO problems.

Method	Bi-TSP20			Bi-TSP50			Bi-TSP100		
	HV \uparrow	Gap \downarrow	Time \downarrow	HV \uparrow	Gap \downarrow	Time \downarrow	HV \uparrow	Gap \downarrow	Time \downarrow
WS-LKH (101 pref.)	0.6268	0.70%	4.2m	0.6401	0.47%	41m	0.7071	-0.06%	2.6h
PPLS/D-C (200 iter.)	0.6256	0.89%	25m	0.6282	2.32%	2.7h	0.6845	3.14%	11h
NSGAII-TSP	0.5941	5.88%	40m	0.5984	6.95%	43m	0.6643	6.00%	53m
DRL-MOA (101 models)	0.6257	0.87%	7s	0.6360	1.10%	10s	0.6971	1.36%	22s
PMOCO (101 pref.)	0.6266	0.73%	8s	0.6349	1.28%	13s	0.6953	1.61%	21s
NHDE-P (101 pref.)	0.6288	0.38%	4.3m	0.6389	0.65%	8.3m	0.7005	0.88%	16m
CDE-alter (101 pref.)	0.6301	0.17%	18s	0.6394	0.58%	23s	0.7009	0.82%	31s
EMNH (aug.)	0.6271	0.65%	1.3m	0.6408	0.36%	4.6m	0.7023	0.62%	17m
PMOCO (101 pref. & aug.)	0.6273	0.62%	46s	0.6392	0.61%	3.1m	0.6997	0.99%	5.7m
NHDE-P (101 pref. & aug.)	0.6296	0.25%	9.8m	<u>0.6429</u>	<u>0.03%</u>	19m	0.7050	0.24%	40m
CDE-alter (101 pref. & aug.)	0.6312	0.00%	1.2m	0.6431	0.00%	4.5m	<u>0.7067</u>	<u>0.00%</u>	6.8m
Method	Bi-CVRP20			Bi-CVRP50			Bi-CVRP100		
PPLS/D-C (200 iter.)	0.3351	3.98%	1.2h	0.4149	3.31%	9.6h	0.4083	1.80%	37h
NSGAII-CVRP	0.3123	10.52%	37m	0.3631	15.38%	38m	0.3538	14.91%	43m
DRL-MOA (101 models)	0.3453	1.06%	7s	0.4270	0.49%	20s	0.4176	-0.43%	40s
PMOCO (101 pref.)	0.3467	0.66%	8s	0.4271	0.47%	18s	0.4131	0.65%	36s
NHDE-P (101 pref.)	0.3458	0.92%	1.5m	0.4248	1.00%	3.1m	0.4127	0.75%	5.3m
CDE-alter (101 pref.)	0.3468	0.63%	17s	0.4272	0.44%	31s	0.4140	0.43%	58s
EMNH (aug.)	0.3471	0.54%	33s	0.4250	0.96%	1.4m	0.4146	0.29%	3.7m
PMOCO (101 pref. & aug.)	<u>0.3481</u>	<u>0.26%</u>	1m	<u>0.4287</u>	<u>0.09%</u>	2.1m	0.4150	0.19%	4.5m
NHDE-P (101 pref. & aug.)	0.3465	0.72%	5.1m	0.4262	0.68%	9.2m	0.4139	0.46%	21m
CDE-alter (101 pref. & aug.)	0.3490	0.00%	2.2m	0.4291	0.00%	4.1m	0.4158	<u>0.00%</u>	6.8m
Method	Bi-KP50			Bi-KP100			Bi-KP200		
WS-DP (101 pref.)	0.3563	0.83%	9.5m	0.4531	1.03%	1.2h	0.3599	2.20%	3.7h
PPLS/D-C (200 iter.)	0.3528	1.81 %	18m	0.4480	2.14%	46m	0.3541	3.78%	1.4h
NSGAII-KP	0.3112	13.39%	30m	0.3514	23.24%	31m	0.3511	4.59%	33m
EMNH	0.3561	0.89%	17s	0.4535	0.94%	53s	0.3603	2.09%	2.3m
DRL-MOA (101 models)	0.3559	0.95%	8s	0.4531	1.03%	13s	0.3601	2.15%	1.1m
PMOCO (101 pref.)	0.3552	1.14%	13s	0.4522	1.22%	19s	0.3595	2.31%	50s
NHDE-P (101 pref.)	<u>0.3564</u>	<u>0.81%</u>	1.1m	<u>0.4541</u>	<u>0.81%</u>	2.5m	<u>0.3612</u>	<u>1.85%</u>	5.3m
CDE-alter (101 pref.)	0.3593	0.00%	21s	0.4578	0.00%	33s	0.3680	0.00%	1.4m
Method	Tri-TSP20			Tri-TSP50			Tri-TSP100		
WS-LKH (210 pref.)	0.4718	1.34%	20m	0.4493	2.30%	3.3h	0.5160	1.02%	11h
PPLS/D-C (200 iter.)	0.4698	1.76%	1.3h	0.4174	9.24%	3.8h	0.4376	16.06%	13h
NSGAII-TSP	0.4216	11.84%	2.1h	0.4130	10.20%	2.3h	0.4291	17.69%	2.5h
DRL-MOA (1035 models)	0.4712	1.46%	51s	0.4396	4.41%	1.5s	0.4915	5.72%	3.1s
PMOCO (10201 pref.)	0.4749	0.69%	8.9m	0.4489	2.39%	17m	0.5102	2.13%	34m
NHDE-P (10201 pref.)	0.4764	0.38%	53m	0.4513	1.87%	1.8h	0.5118	1.82%	4.3h
CDE-alter (10201 pref.)	0.4773	0.19%	10m	0.4517	1.78%	19m	0.5121	1.76%	41m
EMNH (aug.)	0.4712	1.46%	7.1m	0.4418	3.94%	58m	0.4973	4.60%	2.4h
PMOCO (10201 pref. & aug.)	0.4757	0.52%	20m	0.4573	0.57%	1.1h	0.5123	1.73%	4.3h
NHDE-P (10201 pref. & aug.)	<u>0.4772</u>	<u>0.21%</u>	2.1h	<u>0.4595</u>	<u>0.09%</u>	6.7h	<u>0.5210</u>	<u>0.06%</u>	15.3h
CDE-alter (10201 pref. & aug.)	0.4782	0.00%	26m	0.4599	0.00%	1.3h	0.5213	0.00%	4.8h

We present the results of various P' on Bi-TSP50 and Tri-TSP100 in Figure 5 (a) (b). As shown, $P' = 5$ and $P' = 10$ cause inferior performance, while proper P' ($20 \leq P' \leq 40$) results in desirable performance. Intuitively, when limiting the same total gradient steps in training, a larger P' means fewer instances are used for model training. In this sense, too large P' , i.e., with insufficient instances, could lead to inferior performance for solving unseen instances. On the other hand, although the approximate HV is an unbiased estimation, when P' is too small, the calculated variance will become larger, which will also prevent the model from learning favorable global information and thus deteriorate the final performance. Hence we choose $P' = 20$ in this paper.

Figure 5 (c) (d) displays the results of various values of c . As has been presented in Section 4.5, the potential energy function is as Eq. 17, c is a parameter that influences the result former literature (Blank et al., 2020) has reported that c is a weak parameter, because the result does not change a lot when c varies, and the selection of this parameter is only related to the dimension of the objective space. In this part, an experiment is conducted to study the influence of c on Bi-TSP50 and Tri-TSP100 in Figure 5 (c) (d), the results also support the proposition of former researches. So, in this paper, we recommend to use $c = 2m$ in LSS.

Table 5. Experimental results on 200 random instances for MOCO problems.

Type	Method	Bi-TSP150			Bi-TSP200		
		HV \uparrow	Gap \downarrow	Time \downarrow	HV \uparrow	Gap \downarrow	Time \downarrow
Traditional heuristics	WS-LKH (101 pref.)	0.7075	-0.77%	6.4h	0.7435	-1.31%	13h
	PPLS/D-C (200 iter.)	0.6784	3.38%	21h	0.7106	3.17%	32h
	NSGAII-TSP	0.6125	12.76%	2.1h	0.6318	13.91%	3.7h
Neural heuristics	DRL-MOA (101 models)	0.6901	1.71%	45s	0.7219	1.64%	2.1m
	PMOCO (101 pref.)	0.6912	1.55%	1.4m	0.7231	1.47%	3.1m
	NHDE-P (101 pref.)	0.6964	0.81%	12m	0.7280	0.80%	21m
	CDE-alter (101 pref.)	0.6953	0.97%	2.3m	0.7273	0.90%	4.6m
	CDE (101 pref.)	0.6972	0.70%	2.3m	0.7291	0.65%	4.6m
Neural heuristics augmentation	EMNH (aug.)	0.6983	0.54%	53m	0.7307	0.44%	2.9h
	PMOCO (101 pref. & aug.)	0.6967	0.77%	41m	0.7276	0.86%	2.9h
	NHDE-P (101 pref. & aug.)	0.7012	0.13%	1.3m	0.7324	0.20%	4.6h
	CDE-alter (101 pref. & aug.)	0.7003	0.26%	53m	0.7316	0.31%	1.2h
	CDE (101 pref. & aug.)	0.7021	<u>0.00%</u>	53m	0.7339	<u>0.00%</u>	1.2h

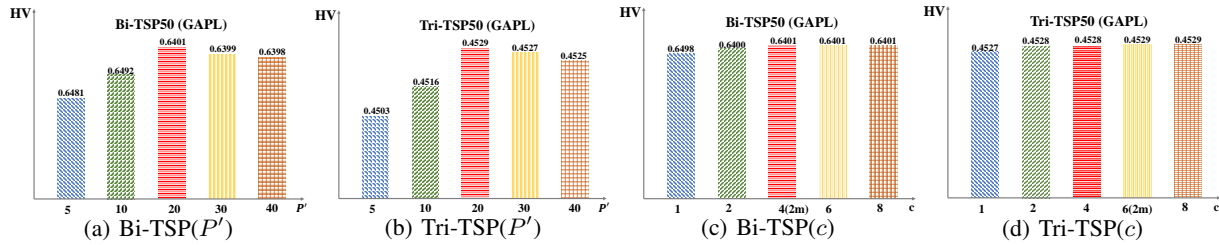


Figure 5. Hyperparameter study. (a) Effect of the maximal size of polar angles pool used in training on Bi-TSP50. (b) Effect of the maximal size of polar angles pool used in training on Tri-TSP100. (c) Effect of the control parameter of potential energy on Bi-TSP50. (d) Effect of the control parameter of potential energy on Tri-TSP50. points from new solutions for updating the Pareto front.

N.4. More Visualization Results for Validity of Context Awareness

We have shown visualization Results of all three classic MOCO problems for each decomposition method in Figure 6. All results can support the conclusion in Section 5.3 to reflect the superiority of CDE’s context awareness.

N.5. Effectiveness of LSSA

We also show the inference time of CDE and CDE w/o LSSA in Figure 7. CDE w/o LSSA adopts traditional LSS. It is evident that LSSA can improve efficiency, as discussed in Section 4.5.

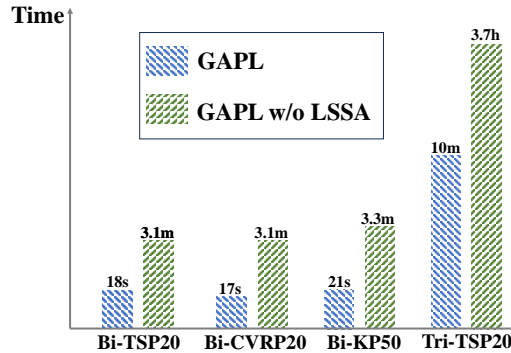


Figure 7. The time consumed by CDE and CDE w/o LSSA.

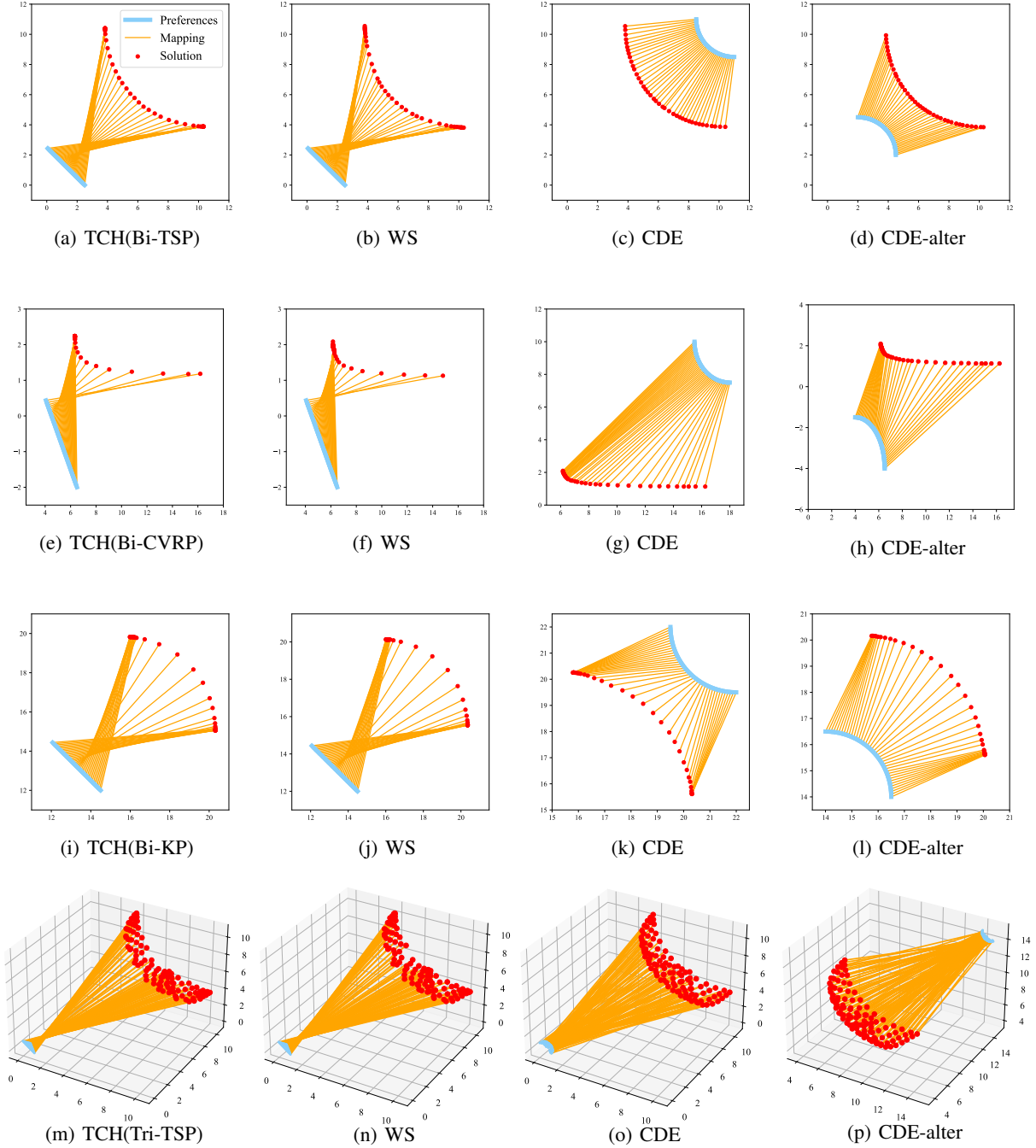


Figure 6. Visual comparisons on Bi-TSP20, Bi-CVRP, Bi-KP20 and Tri-TSP20. CDE and GADL-alter have better adaptability than WS- and TCH-based approaches.

O. Convergence of the Pareto Front Hypervolume

Assuming that $b \leq r_1 - y_i \leq B, \forall i \in \{1, \dots, m\}, y \in Y$. Let $\mathcal{Z}(\theta) = \frac{\Phi}{m^{2m}} \mathcal{V}_X(\theta)^m$, then $\sup_{\theta} \mathcal{Z}(\theta) \leq \frac{\Phi}{m^{2m}} B^m m^{m/2}$. Let $\hat{\mathcal{H}}\mathcal{V}_r(Y) := \frac{1}{P} \sum_{i=1}^P \mathcal{Z}(\theta^{(i)})$ denote the empirical estimation of $\mathcal{H}\mathcal{V}_r(Y)$ with P samples. Via Hoeffding inequality,

similar to (Zhang & Golovin, 2020), we have the following inequality:

$$\Pr(|\hat{\mathcal{H}\mathcal{V}_r}(Y) - \mathcal{H}\mathcal{V}_r(Y)| \geq \epsilon) \leq 2\exp\left(\frac{-P\epsilon^2 2^{m+2}}{\Phi^2 B^{2m} m^{m-2}}\right). \quad (32)$$

P. The bound of $\mathcal{V}_X(\theta)$ in Eq. 11

Since $\mathcal{V}_X(\theta)$ is a max-min problem, we can conclude that the following inequalities hold:

$$\mathcal{V}_X(\theta) \leq Bm^{\frac{1}{2}}, \quad (33)$$

where $b \leq (r_i - f_i(\mathbf{x})) \leq B, \forall \mathbf{x} \in \mathcal{X}, \forall i \in \{1, \dots, m\}$ and $\|\lambda\|_2 = 1$.

Proof.

$$\begin{aligned} \mathcal{V}_X(\theta) &\leq \max_{\mathbf{x} \in \mathcal{X}, \|\lambda\|_2=1} \left(\min_{i \in \{1, \dots, m\}} \left\{ \frac{r_i - f_i(\mathbf{x})}{\lambda_i(\theta)} \right\} \right) \\ &\quad (r_i - f_i(\mathbf{x}) \leq B) \\ &\leq \max_{\|\lambda\|_2=1} \left(\min_{i \in \{1, \dots, m\}} \left\{ \frac{B}{\lambda_i(\theta)} \right\} \right) \\ &\leq \frac{B}{m^{-\frac{1}{2}}} \\ &= Bm^{\frac{1}{2}}. \end{aligned} \quad (34)$$

The transition from line one to line two is due to the fact that the inequality $r_i - f_i(\mathbf{x}) \leq B$ holds for $\forall \mathbf{x} \in \mathcal{X}$ and for $\forall i \in \{1, \dots, m\}$. The transition from line two to line three is $\max_{\|\lambda\|_2=1} \left(\min_{i \in \{1, \dots, m\}} \left\{ \frac{B}{\lambda_i(\theta)} \right\} \right)$ is an optimization problem under the constraint $\|\lambda\|_2 = 1$. The upper bound for this optimization is when $\lambda_1 = \dots = \lambda_m = m^{-\frac{1}{2}}$. \square

Q. Equivalence of Hypervolume Calculation in Polar Coordinates

Proof. $\mathcal{H}\mathcal{V}_r(Y)$ can be simplified by the following equations. Here Ω denoted the dominated regions by the Pareto front, i.e., $\mathcal{H}\mathcal{V}_r(Y) = \Lambda(\Omega, \mathbf{r})$.

$$\begin{aligned} \mathcal{H}\mathcal{V}_r(Y) &= \int_{\mathcal{R}^m} I_{\Omega} dy_1 \dots y_m \\ &\quad ("dv''" \text{ denoted the infinitesimal sector area.}) \\ &= \underbrace{\int_0^{\frac{\pi}{2}} \dots \int_0^{\frac{\pi}{2}}}_{m-1} dv \\ &\quad ("dv''" \text{ equals the angle ratio multiplied by } \mathcal{V}_X(\theta)^m \text{ multiplied by the unit for volume.}) \\ &= \underbrace{\int_0^{\frac{\pi}{2}} \dots \int_0^{\frac{\pi}{2}}}_{m-1} \frac{\Phi}{m} \cdot \frac{\mathcal{V}_X(\theta)^m}{2\pi \cdot \pi^{m-2}} \underbrace{d\theta_1 \dots \theta_{m-1}}_{d\theta} \\ &= \frac{\Phi}{2m\pi^{m-1}} \underbrace{\int_0^{\frac{\pi}{2}} \dots \int_0^{\frac{\pi}{2}}}_{m-1} \mathcal{V}_X(\theta)^m d\theta \\ &= \frac{\Phi}{2m\pi^{m-1}} \cdot \frac{\pi^{m-1}}{2} \cdot \mathbb{E}_{\theta}[\mathcal{V}_X(\theta)^m] \\ &= \frac{\Phi}{m2^m} [\mathcal{V}_X(\theta)^m]. \end{aligned} \quad (35)$$

We specify $\theta \sim \text{Unif}(\Theta) = \text{Unif}([0, \frac{\pi}{2}]^{m-1})$ in Eq. 35.

Line 2 holds since it represents the integral of Ω expressed in polar coordinates, where in the element dv corresponds to the volume associated with a segment obtained by varying $d\theta$.

Line 3 calculates the infinitesimal volume of dv by noticing the fact that the ratio of dv to $\frac{\Phi}{m}$ is $\frac{\mathcal{V}_X(\theta)^m}{2\pi \cdot \pi^{m-2}}$. Line 4 is a simplification of Line 3. And Line 5 and 6 express the integral in its expectation form. \square

R. Licenses

The licenses for the codes we used in this work are shown in Table 6.

Table 6. List of licenses for the codes suite we used in this work.

Resources	Type	Link	License
PSL-MOCO (Lin et al., 2022)	Code	https://github.com/Xi-L/PMOCO	MIT License
NHDE (Chen et al., 2023b)	Code	https://github.com/Bill-CJB/NHDE	MIT License
EMNH (Chen et al., 2023a)	Code	https://github.com/Bill-CJB/EMNH	MIT License